WATER JET EROSION BEHAVIOR OF HVOF SPRAYED Cr_3C_2-NiCr COATINGS ON STAINLESS STEEL

[1] K. Arunkumar
Research Scholar**,**
Department of Mechanical Engineering, Government College of Engineering,
Bargur– 635104, Krishnagiri. Tamil Nadu, India.
Email: mecharun59@gmail.com ; Tel: +91-09995453358(Mobile)

[2]D. Thirumalaikumarasamy (**Corresponding Author**)*
Assistant Professor,
Department of Mechanical Engineering, Government College of Engineering,
Bargur– 635104, Krishnagiri. Tamil Nadu, INDIA.
Email: tkumarasamy412@gmail.com
Tel: +91-09894319865(Mobile) ; Fax: +91-4144-238080/238275

[3]P. Thirumal
Associate Professor,
Department of Mechanical Engineering, Government College of Engineering,
Bargur– 635104, Krishnagiri. Tamil Nadu, INDIA.
Email: ptml76@gmail.com ; Tel: +91-09443455580(Mobile)

Abstract

Due to the high temperature wear resistance, low friction coefficient and corrosion resistance, chromium carbides are widely used for coating applications and commonly processed through thermal spraying. High velocity thermal spray cermet coatings are widely used to mitigate wear at high temperatures and in corrosive environments due to their superior oxidation and corrosion resistance. Coatings based on Cr_3C_2-NiCr have been deposited by means of the HVOF thermal spraying technique on a AISI 404 steel substrate. Furthermore, the erosion behavior of the substrate and coated samples were carried out using water jet erosion test. The effect of water jet parameters including angle of impingement, water jet velocity, stand of distance and erodent discharge was systematically investigated on the erosion rate. The experiments were performed based on central composite design and response surface method to develop multiple regression models. The accuracy of the regression models was adequate through analysis of variance to make correlations between input parameters and responses. Results indicated that angle of impingement was the most predominant factor affecting the erosion rate of the coatings followed by water jet velocity, standoff distance and erodent discharge.

Keywords: *Erosion; Cr_3C_2-NiCr; HVOF; RSM*

Abbreviations:
HVOF: High velocity oxy fuel
RSM: Response surface methodology

1.0 Introduction

Despite tremendous developments in the marine component design and material improvements, liquid jet impingement erosion still remains an unsolved problem. This phenomenon occurs in all the marine components: (a) propellers, hubs and rudders in case of ships, (b) high-speed pumps of all types, (c) regulators, valves and gate valves, (d) flow measuring equipment like orifices and ventures, (e) sudden enlargements and bends, etc. The marine components machinery has to tolerate perpetual high speed water (with or without solid particles) impingement, and hence they must have excellent strength, toughness and erosion resistance. Naval application components are damaged under high speed water (with or without solid particles) impingement, thus interrupting smooth functioning of system. Hence, it is important to develop more erosion resistant system to combat water jet erosion.

The blades of large centrifugal air compressor impellers operating under marine environment are generally subject to corrosion from the salty coastal air and erosion of solid particles, commonly resulting in corrosion rust and erosion wear [1, 2]. Therefore, the improvement of the corrosion and the erosion resistance of the impeller blades by using surface treatment technology is crucial. To date, scholars have found that the thermal spraying technology is an effective method for improving surface functionality [3] due to its advantages, such as minor thermal stress and small heat-affected zone. Therefore, the interaction mechanism between erosion and corrosion of coatings is an important research topic.

Thermal sprayed cermet coatings have been widely used for the improvement of wear resistance and wear repairing of key components in some fields, such as aerospace, petrochemical, machinery manufacturing, automobile transportation, ferrous metallurgy and marine equipment. Chromium carbide has been widely used as one of the metal carbides due to its high hardness, high melting point, high elastic modulus, great chemical corrosion resistance and wear resistance [4]. The thermal sprayed Cr_3C_2-NiCr has been successfully applied for surface protection and modification in the fields of aerospace, automobile, energy, etc. due to high temperature wear resistance, corrosion resistance and high hardness [5, 6]. The chromium carbide coatings provide excellent resistance to high-temperature oxidation (up to 750°C) and reduce the decrease in the coating properties such as wear resistance and hardness due to the formation of the Cr_2O_3 on its surface [7]. Therefore, high temperature wear protection applications are served by chromium carbide based hard metals, mainly Cr_3C_2-NiCr with 20–25 wt% binder phase. Among various thermal spray technologies, high velocity oxy-fuel (HVOF) offers excellent micro hardness, good adhesion between splats and minimum porosity of the coated specimens. Nowadays, Cr_3C_2-NiCr is almost exclusively deposited by means of high velocity oxygen-fuel (HVOF) spraying [8].

Thermally sprayed Cr_3C_2-NiCr coatings have been widely used in the fields of aerospace,

petrochemical engineering, and marine engineering equipment due to its resistance against corrosion [9], wear [10], and erosion [11]. The mechanical properties [12], deposition behavior [13], and wear behavior [14] of Cr_3C_2-NiCr coatings have been widely investigated under varying circumstances (damage mode, particle size, and temperature). The protection of the substrate from corrosion by applying the cermet coatings is a promising method. However, the corrosion performance is strongly related to porosity, which introduces the corrosion channel, especially in coatings without proper or destroyed sealing. Galvanic corrosion between the coating and the substrate may take place in the presence of corrosion channels. Such channels accelerate the corrosion of the substrate. The interface between the coating and the steel substrate corrodes remarkably in the non sealing-treated specimens and the corrosion of the coating is relatively restrained as the substrate acts as an anode. The corrosion resistance of coatings varies with porosity, which likely affects the erosion resistance of cermet coatings. Porosity is clearly a dominant factor affecting the erosion and corrosion performance [9-14]. However, the water jet erosion behavior of thermal sprayed coatings has rarely been reported. Therefore, in this work, an attempt has been made to develop empirical relationship connecting the water jet erosion input parameters angle of impingement, water jet velocity, stand of distance and erodent discharge and the output response of erosion rate by RSM.

2. Experimental

In this study, conventional powders were used for depositing Cr_3C_2-NiCr coatings with the thickness of about 200 μm on a stainless steel 304 substrate by HVOF (HIPOJET-2700, Make: Metallizing Equipment Co. Jodhpur, India) system available at Annamalai University, India. The thickness of the coatings was measured by digital micrometer (with an accuracy of 0.001mm) after each and every run conditions. Coating thickness was achieved by varying the number of deposition passes. Photograph of HVOF spray machine and the coated specimens were shown in Fig.1. The substrate needs to be preheated before spraying: this was accomplished through one complete torch cycle at a pass velocity of 0.8 m/s, achieving a temperature of 120–180°C. The substrate samples with the size of 20 mm × 20 mm × 6 mm, whose sides had a chamfer with a length of 1 mm and an angle of 45°, were cleaned in acetone by ultrasonic cleaning instrument. Corundum, grit size of 320 ± 500 μm was used to increase the surface roughness of the substrate. A surface roughness tester (Make: Mitutoyo, Japan; Model: Surf test 301) was used to measure the roughness and the average roughness of the substrate after grit blasting was found to be 5-10 μm.

(a) Before Coating **(b) After Coating**

(c) HVOF Spray Facility
Fig.1 Experimental

The micro morphology of coatings was observed using SEM (Make: JEOL, Japan; Model: 6410-LV).The X-ray diffraction (XRD) patterns of coatings were analyzed on the coating surface by using the Rigaku DMAX-2500PC diffract meter and Cu-Kα radiation over an angular range of $20° \leq 2\theta \leq 90°$. According to the ASTM B 276 [15], the porosity measurement was carried out on the metallographically prepared cross-sections of the coating, using optical microscope (Make: Meiji; Japan, Model: MIL-7100) equipped with an image analyzing software (Metal Vision version.6). The micro hardness of the cross section was tested using the Vickers hardness tester (Make: Shimadzu; Japan. Model: HMV-2T). Hardness values were measured at10 random locations on the polished cross-section of a coating.) at a load of 300 g (10 seconds).

2.1 Water jet erosion testing

Water jet erosion mass loss of the coated and uncoated specimens was determined using water jet erosion tester (Model: TR- 411, Make: DUCOM, India) to explore the effect of angle of impingement, water jet velocity, stand of distance and erodent discharge on the erosion behaviours. The test is carried out by measuring the loss of mass of the specimen by weighing it before and after the process in the tester (Fig. 2). Specimens were polished ultrasonically cleaned using acetone and weighed prior to test and post-test to find weight loss from which the erosive wear was calculated. . Specimens were polished ultrasonically cleaned using acetone and weighed prior to test and post-test to find weight loss from which the erosive wear was calculated. The specimen to be tested is first thoroughly cleaned and weighed in using a precision weighing machine. These specimens having a standard size are fixed onto the disc with the help of clamps at the desired radial distance. The disc along with the specimen is dipped into the slurry contained in the container. The motor is then started and the specimens are rotated at the desired speed for a given duration. The specimen is removed, cleaned and weighed after the test is completed. The rate of erosion is calculated at the rate of loss of mass with respect to various experimental parameters. Erodent used in the water jet erosion and slurry erosion tests was Quartz sand of 50 μm sizes and its SEM image is shown in Fig. 3.

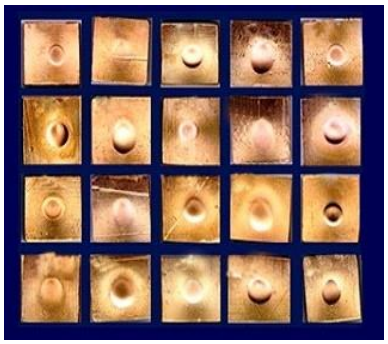

(a) Uncoated specimens after test

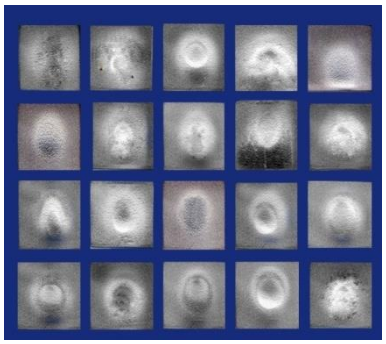

(b) Coated specimens after test

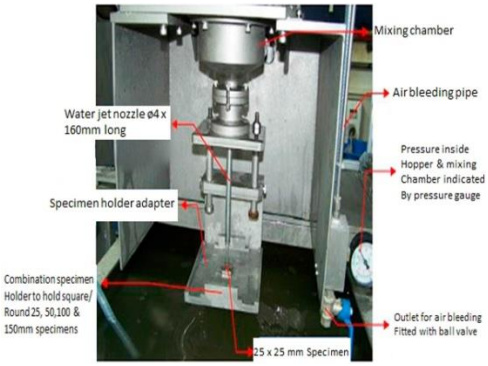

(C) Water jet erosion test setup

Fig. 2 Photographs of specimens before and after test

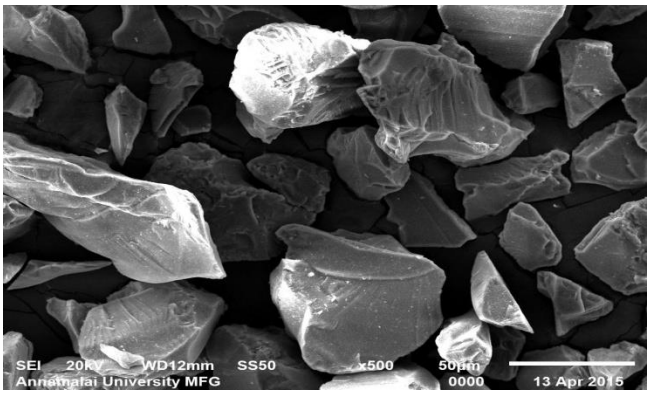

Fig.3 SEM micrograph of erodent particles

2.2 Coating characterization

The SEM analysis of the coating powder is shown in Fig. 4a. The Cr_3C_2–NiCr powder is characterized by porous structure with particles consisting of micron-sized granular microstructure. Fig. 4b shows the SEM micrograph of a cross section of the as sprayed coating. It is recognizable that the coating exhibits a dense and homogenous microstructure with a porosity of less than porosity 2%.

The pores and microcracks were not observed at the interface to the substrate. The SEM micrograph shows that dark carbide particles are distributed uniformly within the coating. Some carbides exhibit partly rounded boundaries, indicating that they were partly melted during

spraying. Varying intensity of grey scales of carbides in the figure can be attributed to the variation of carbon contents in the carbides. Fig. 5 reveals the XRD-diffraction patterns of the spray powder and the coating. Strong peaks of the phase Cr_3C_2 are recognizable in the coating. It is assumed that Cr_7C_3 is formed due to decarburization of Cr_3C_2 during spraying.

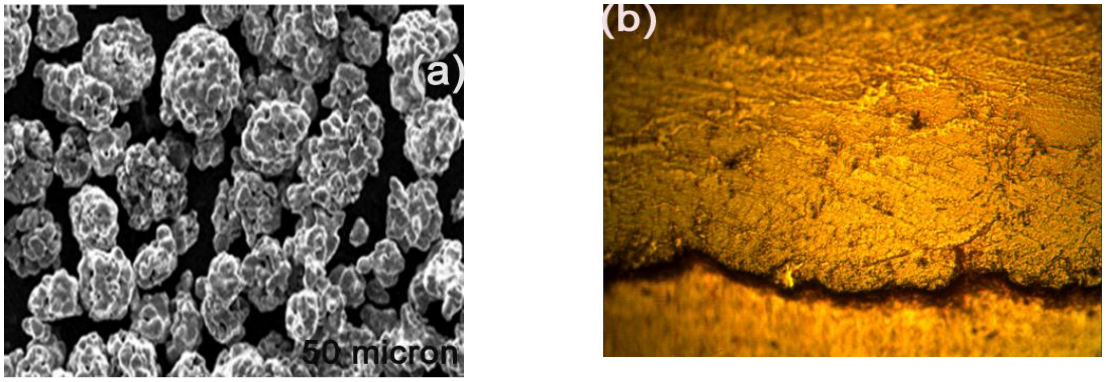

Fig.4 (a) SEM micrograph of Cr_3C_2-NiCr powder and (b) cross section of the as sprayed coating

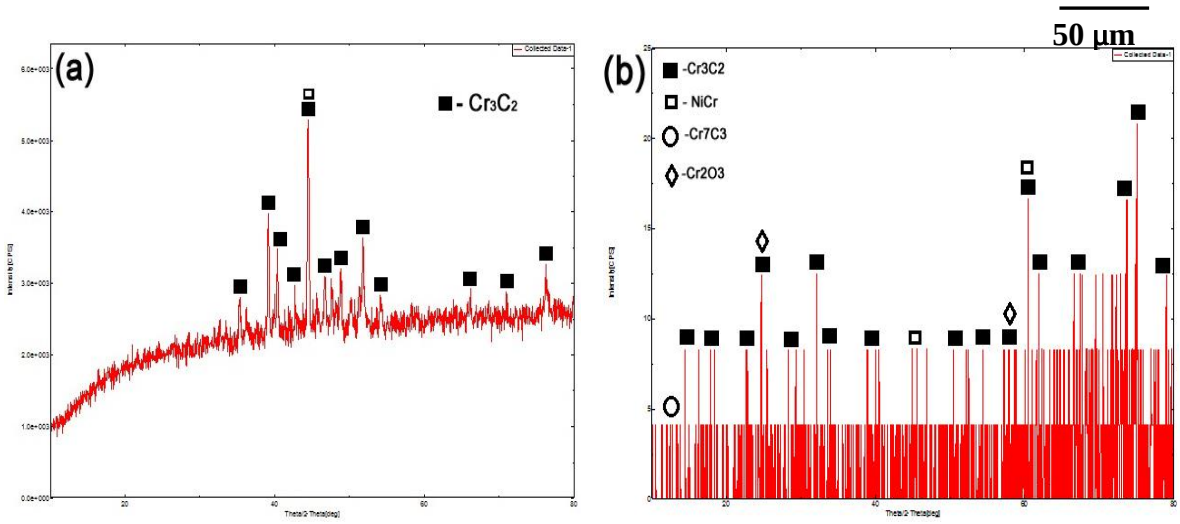

Fig.5 X-ray diffraction patterns of the spray powder (a) and the as-sprayed coating (b)

2.3 Formulating Experimental Design Matrix to Conduct the Erosion Tests

After considering all of the feasible limits of the water jet erosion testing parameters, their limits were chosen, so that erosive test could be conducted without any difficulty. A central composite rotatable design of second order was used (RSM) to establish the empirical relationship between the parameters using the smallest possible number of experiments without a loss of accuracy. [16] The factors and their ranges considered for the erosion test are shown in Table 1. Table 2 shows the experimental results of the water jet erosion tests for both coated and uncoated stainless steel.

Table 1 Water jet erosion test parameters and their levels

S.No	Factors	Notations	Units	Levels

				-2	-1	0	1	2
1	Angle of impingement	A	deg	30	45	60	75	90
2	Water jet velocity	V	m/s	10	20	30	40	50
3	Stand-off distance	D	mm	35	40	45	50	55
4	Erodent discharge	F	gpm	500	1000	1500	2000	2500

Table 2. Experimental design matrix and results

	Variables (factors)				**Responses**	
Exp. condition	**Angle of impingement (A) deg**	**Water jet velocity (V) m/s**	**Stand-off distance (D) mm**	**Erodent discharge (F gpm**	**Mass loss of uncoated substrate (g)**	**Mass loss of coatings (g)**
1	45	2040	1000		0.0881	0.033
2	75	2040	1000		0.0594	0.0223
3	45	4040	1000		0.2603	0.0976
4	75	4040	1000		0.2689	0.1008
5	45	2050	1000		0.0986	0.037
6	75	2050	1000		0.0841	0.0315
7	45	4050	1000		0.2604	0.0977
8	75	4050	1000		0.2884	0.1082
9	45	2040	2000		0.0381	0.0143
10	75	2040	2000		0.0434	0.0163
11	45	4040	2000		0.2104	0.0789
12	75	4040	2000		0.2613	0.098
13	45	2050	2000		0.0589	0.0221
14	75	2050	2000		0.0773	0.029
15	45	4050	2000		0.2197	0.0824
16	75	4050	2000		0.2894	0.1085
17	30	3045	1500		0.1042	0.0391
18	90	3045	1500		0.1411	0.0529
19	60	1045	1500		0.0131	0.0049
20	60	5045	1500		0.3687	0.1383
21	60	3035	1500		0.1302	0.0488
22	60	3055	1500		0.1718	0.0644
23	60	3045	500		0.2103	0.0789
24	60	3045	2500		0.1869	0.0701

25	60	3045	1500	0.13120.0492
26	60	3045	1500	0.13480.0506
27	60	3045	1500	0.12950.0486
28	60	3045	1500	0.13070.049
29	60	3045	1500	0.12470.0468
30	60	3045	1500	0.13610.051

3.0 Predictive Statistical Model for Erosion rate

In the present investigation, to correlate the experimental parameters and the wear rate, a linear quadratic empirical relationship was developed to predict the responses based on experimentally measured values. The responses are function of angle of impingement (A), water jet velocity (V), stand of distance (D) and erodent discharge (F) it can be expressed as,

Responses = f (A, V, D, F) …….. (1)

In this work, the regression coefficients were calculated with the help of Design Expert V 8.1 statistical software. After determining the significant coefficients (at a 95% confidence level), the final empirical relationships were developed using these coefficients. The final empirical relationships to estimate the wear rate are,

Mass loss of uncoated stainless steel (gpm) = $\{0.23 – 0.038\ (A) - 0.7X10^{-3}\ (V) – 0.039\ (D) – 0.025\ (F)\}$ …….. (2)

Mass loss of coated stainless steel (gpm) = $\{0.029 + 4.14\times10^{-3}\ (A) + 6.4\times10^{-3}\ (V) + 8.4\times10^{-3}\ (D) – 2.7\times10^{-4}\ (F)\}$. ……..(3)

3.1 Checking the Adequacy of the Formulated Empirical Relationships

In this investigation, analysis of variance (ANOVA) technique is used to check the adequacy of the developed empirical relationships. ANOVA test results of the erosion rate of uncoated stainless steel and coated stainless steel are presented in Tables 3 and 4 respectively. The procedure for interpreting the ANOVA data is available in the literature [17]. From the F value assessment, it was found that the predominant factors which have a direct influence on the responses as per hierarchy are angle of impingement, jet velocity, stand-off distance and erodent discharge. The determination coefficient (R^2) indicates the goodness-of-fit for the model. It is inferred from the ANOVA results, the developed model is significant and lack of fit is not significant. Hence, the developed empirical relationships can be effectively used to predict the responses by substituting the experimental parameter values in coded form as it is desired.

Table 3 ANOVA results for uncoated stainless steel

Source	Sum of Squares	df	Mean square	F Value	p-value Prob> F	
Model	3.105×10^{-3}	4	7.763×10^{-4}	48.81	< 0.0001	Significant
Angle of impingement	1.862×10^{-3}	1	1.862×10^{-3}	117.10	< 0.0001	
Jet velocity	8.777×10^{-4}	1	8.777×10^{-4}	55.18	< 0.0001	
Stand-off distance	4.461×10^{-4}	1	4.461×10^{-4}	28.05	< 0.0001	
Erodent Discharge	1.050×10^{-5}	1	1.050×10^{-5}	0.66	0.4243	
Residual	3.976×10^{-4}	25	1.590×10^{-5}			
Lack of Fit	3.468×10^{-4}	21	1.651×10^{-5}	1.30	0.4431	Not significant
Pure Error	5.085×10^{-5}	4	1.271×10^{-5}			
Core Total	3.503×10^{-3}	29	$R^2 = 0.9987$			

df: degrees of freedom: CV: co-efficient of variation; F: Fisher ratio; p: probability,

Table 4 ANOVA results for coated stainless steel

Source	Sum of Squares	df	Mean square	F Value	p-value Prob> F	
Model	3.036×10^{-3}	4	7.589×10^{-4}	1419.81	< 0.0001	Significant
Angle of impingement	1.840×10^{-3}	1	1.840×10^{-3}	3441.47	< 0.0001	
Jet velocity	9.346×10^{-4}	1	9.346×10^{-4}	1748.42	< 0.0001	
Stand-off distance	4.067×10^{-4}	1	4.067×10^{-4}	760.87	< 0.0001	
Erodent Discharge	2.396×10^{-6}	1	2.396×10^{-6}	4.48	0.0444	
Residual	1.336×10^{-5}	25	5.345×10^{-7}			
Lack of Fit	1.286×10^{-5}	21	6.125×10^{-7}	4.90	0.0667	Not significant
Pure Error	5.000×10^{-7}	4	1.250×10^{-7}			
Core Total	3.049×10^{-3}	29	$R^2 = 0.9942$			

df: degrees of freedom: CV: co-efficient of variation; F: Fisher ratio; p: probability

4.0 Results and Discussion

4.1 Effect of water jet experiment parameters on erosion rate

Figure 6 (a- f) demonstrate the interaction effects of water jet erosion test parameters on water jet erosion rates. Figures 6 (a&b) shows the interaction effect of angle of impingement and stand of distance on erosion rate. From these figures, it is inferred that a small change in angle and jet velocity have an impact on water jet erosion rate [18]. However, increasing jet velocity combined with stand-off distance (Fig. 6 b) has major effect on wear rate in uncoated stainless steel and little amount in coated stainless steel because of hardness of the coatings. Low hardness value of stainless steel was severely affected.

Figures 6 (c and d) relates the effect of jet velocity and stand-off distance. From the figures, one can infer that stand-off distance dominating the erosion rate of stainless steel, where as in coated stainless steel system both stand-off distance and jet velocity has a marginal effect. Figures 6 (e-f) discloses the effects of standoff distance and erodent discharge. Varying stand-off distance causes damage in uncoated stainless steel and coated stainless steel system. However, large variations in erodent discharge did not make any significant loss during testing. These results are having well agreement with ANOVA results are presented in tables 3 and 4.

Figures 7 (a-f) illustrate the three dimensional plots of interaction effects of water jet test parameters on erosion rate. The effect of angle impingement and erodent discharge, this combination has significant metal loss due to the metallic nature of stainless steel substrate at lower angles as seen in Figures 7 (a-b). However, material removal is in higher rate at high impact angles in coated stainless steel. Figures 7 (c and d) show the response graph of erosion rate. When the erodent discharge and jet velocity combines erosion loss of these parameters has significant in uncoated stainless steel and erosion rate is minimum in Cr_3C_2 - NiCr coated stainless steel. Figures 7 (e-f) present the interaction effect of stand of distance and erodent discharge. Low velocity with noticeable erodent discharge shows small loss of material. Increasing velocity with higher erodent promotes material loss. The same phenomenon was also observed coated stainless steel.

Uncoated specimens **Coated specimens**

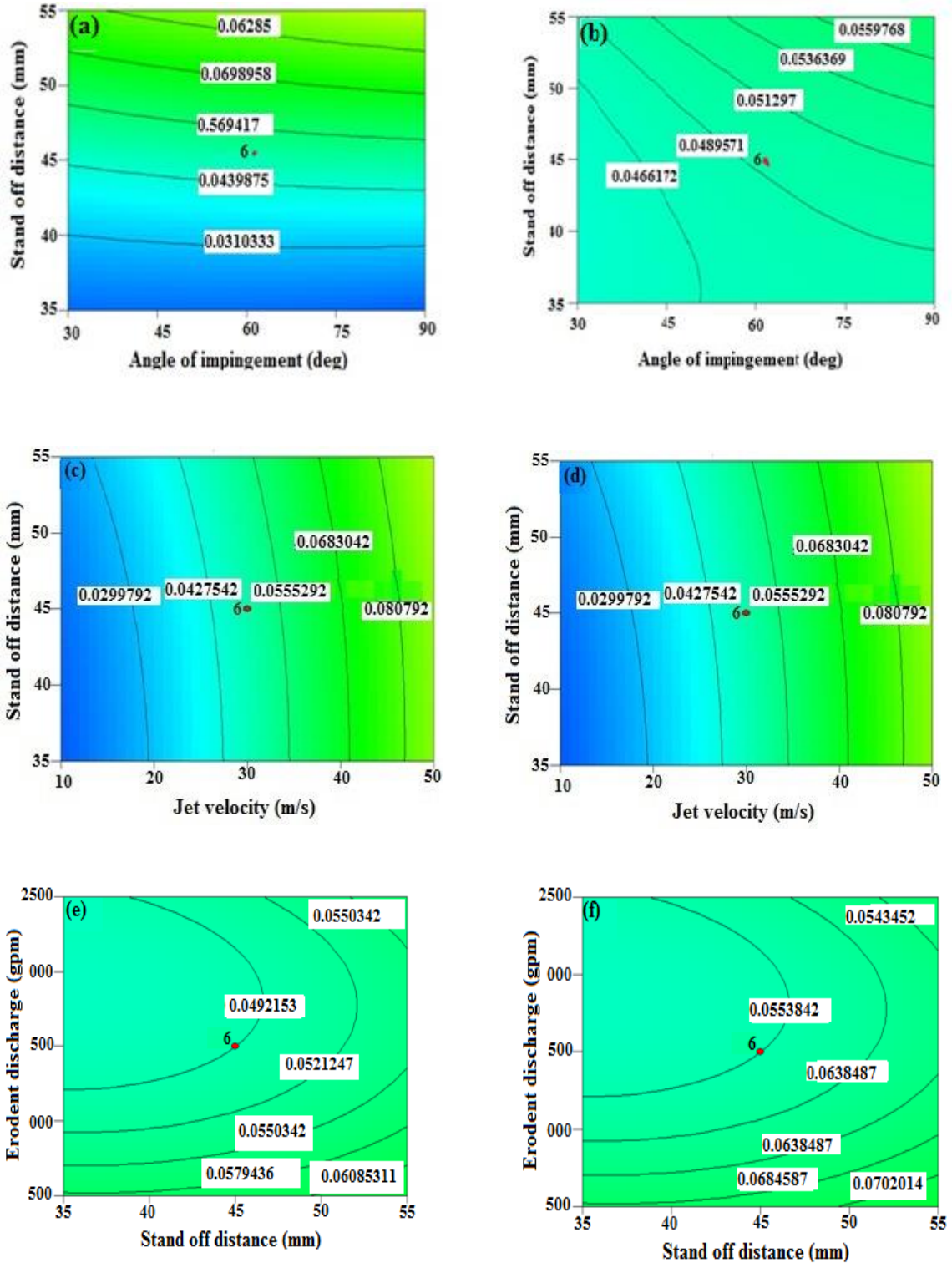

Fig. 6 Two dimensional surface plot of uncoated and coated stainless steel

Uncoated specimens **Coated specimens**

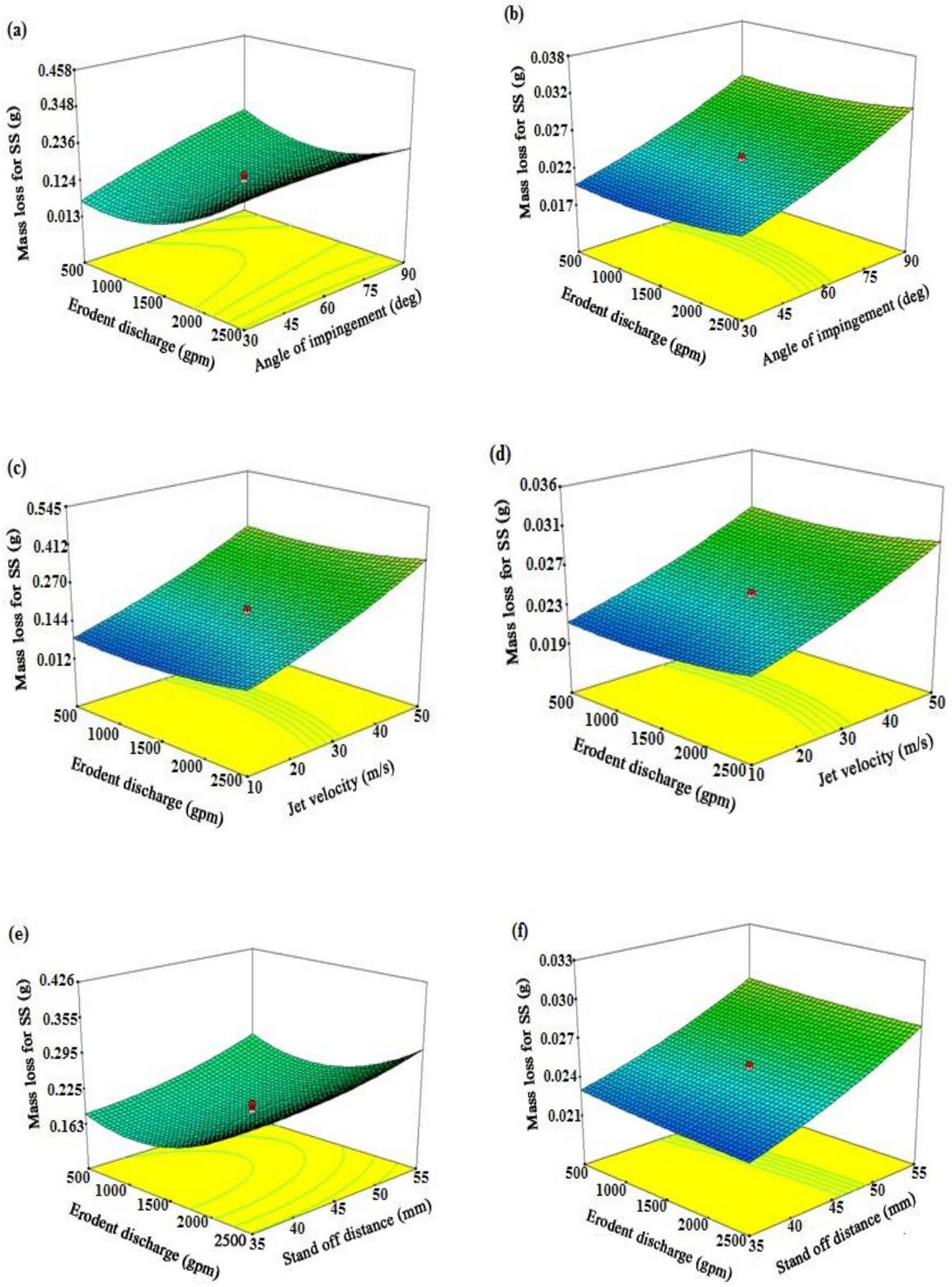

Fig. 7 Three dimensional surface plot of uncoated and coated stainless steel

Figures 8 (a-b) show the perturbation plot for stainless steel substrate and Cr_3C_2 - NiCr coated stainless steel. From the figures, it is inferred that, increasing the angle of impingement on uncoated stainless steel increases wear rate and opposite behavior was observed in coated stainless steel. However, the remaining parameters shows the positive similar trend in wear rate and those parameters are less significant in promoting material loss as observed in the ANOVA tests.

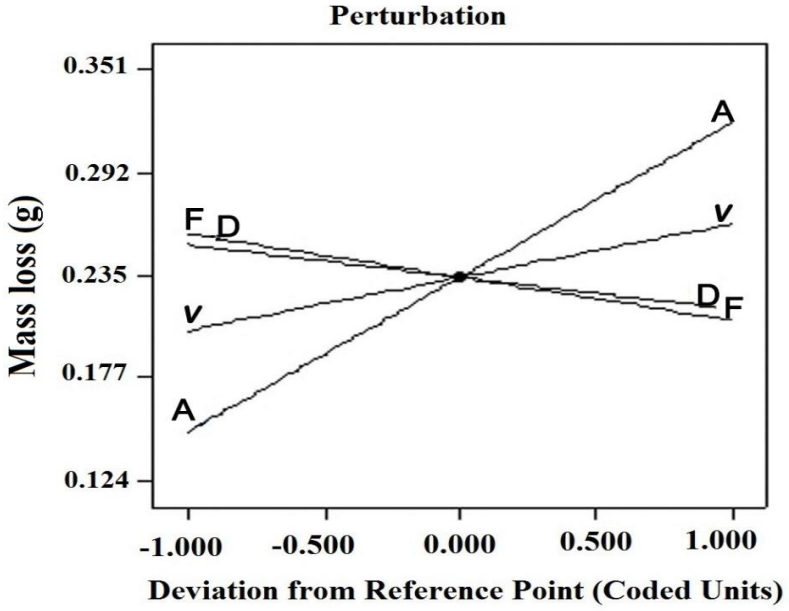

(a) Uncoated stainless steel

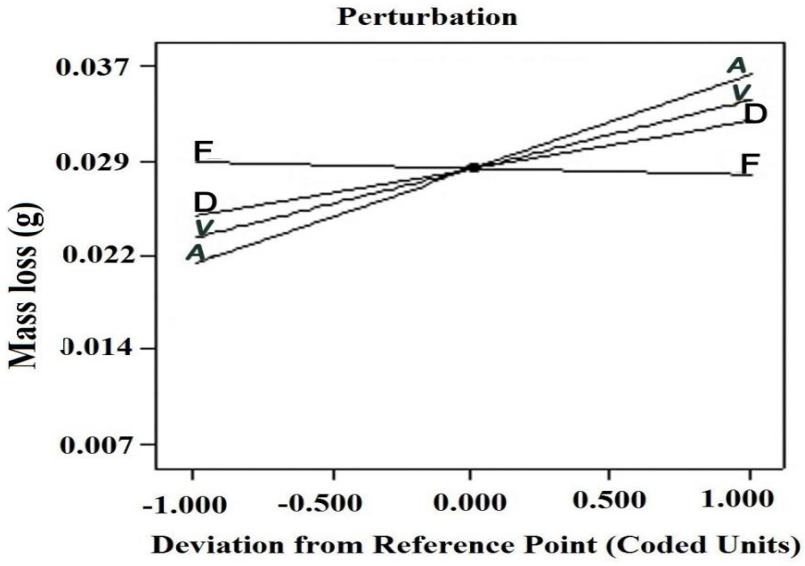

(b) Cr_3C_2 - NiCr coated stainless steel

Fig. 8 Perturbation plots shows the effect of individual parameters on water jet erosion rate

4.2 Effect of water jet velocity on erosion rate

When the velocity of the water jet decreased, the kinetic energy transferred to the particle is

decreased. The lower the kinetic energy, the less the chance of a positive result (the erosion decreases) from a single impact. Further, under low velocities the particle jet divergence increases under such circumstances that promote micro cutting in the uncoated stainless steel as seen in Fig.9 a. The initial impact energy of the particle is expended in deformation as the particle still has a considerable horizontal velocity component when it leaves the metal surface [19, 20]. As the impact energy is lowered, less lateral cracks are generated around the plastic indentation on the lamellae of the carbide coatings as seen in Fig.9 b. At medium jet velocity conditions, moderate impact energy provided to the particles are able to promotes micro cutting in the stainless steel. In the case of the uncoated and coated stainless steel, the low forward momentum of the particle means that it will tend to roll on the target surface resulting in little surface deformation and rub bands are seen in Fig.9c&d. Consequently, material removal in low and medium jet velocity conditions will be minimum. With the higher initial velocity of jet, the erosion rate appears to increase explicitly. This suggests that erosion rate to be nearly proportional to the square of velocity or the kinetic energy of particle. Though not conclusive, it may be due to the fact that larger areas are removed under the higher velocity jet impact as shown in Fig.9 e. The increase in plasticity at high velocities may increase the loss erosion by the fracture of brittle materials, since the irreversible deformation will create an increase in the driving forces for lateral cracking, thereby reducing the resistance to further impacts [21]. It might be expected that the shear force applied by the particle would increase as a result of an increasing contact velocity. The jet divergence also decreases with the increase in velocity. This in turn should result in more material being displaced from under the particle to the front of the crater during impact [22]. The extensive lateral cracking seen at individual impact sites together with the evidence for plastic indentation as seen in Fig.9 f supports this reason. Thus, the possibility of plastic response to erosive impact due to increased surface temperatures may in advertently lead to greater lateral spallation. Atomic microscopic analysis also carried out on the uncoated and coated eroded specimen top surface at low and high velocity conditions. Small trough values are observed at low velocity conditions in both uncoated and coated specimens (Figures 10 a & b). The particles that strike the surface of a ductile material at a velocity greater than the critical velocity needed for the penetration of the material's surface do remove some material, in a process similar to the cutting action of a machine tool. At the impact location on the base material, the particle loses a fraction of its kinetic energy to the target material in the form of heat and energy for deformation of the surface. Very high levels of shear strain may be induced in the material at the impact location [23]. Irreversible deformation, larger area spallation of the coatings makes large undulations on the coated surface. Hence, the roughness of the coatings surface is increased.

Figures 10 (c&d) show the AFM images of various level of jet velocity impacted eroded specimens that shows very high undulations in stainless steel and coatings. Fig.11 compares the mass loss at different velocity levels. It is inferred that increasing velocity increases erosion loss irrespective of the system. Introduction of Cr_3C_2 - NiCr coating over the stainless steel reduces erosion loss about 50 % considerably.

Uncoated specimens **Coated specimens**

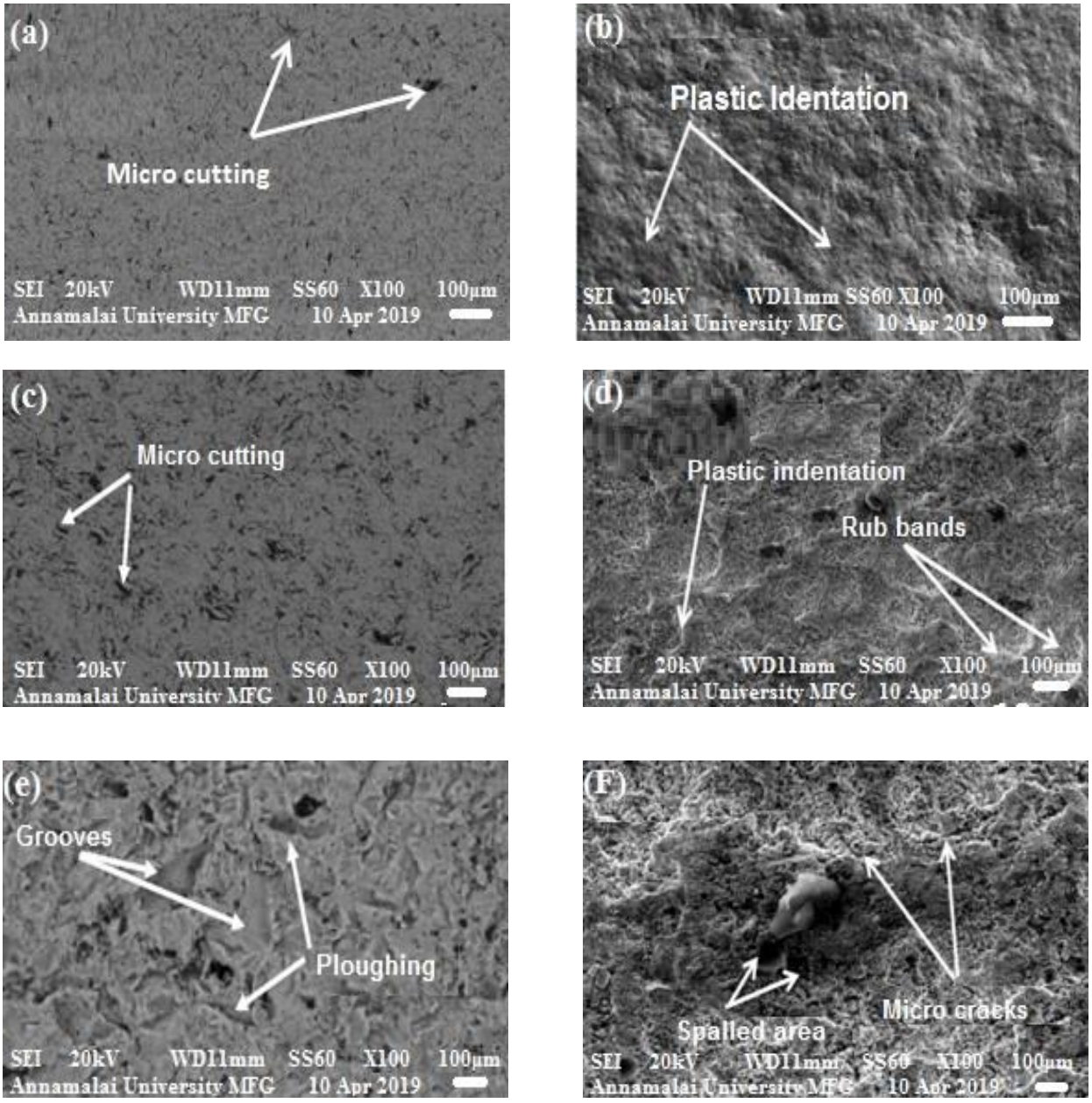

Fig. 9 SEM images of the eroded surface of substrate and coating at various water jet velocities

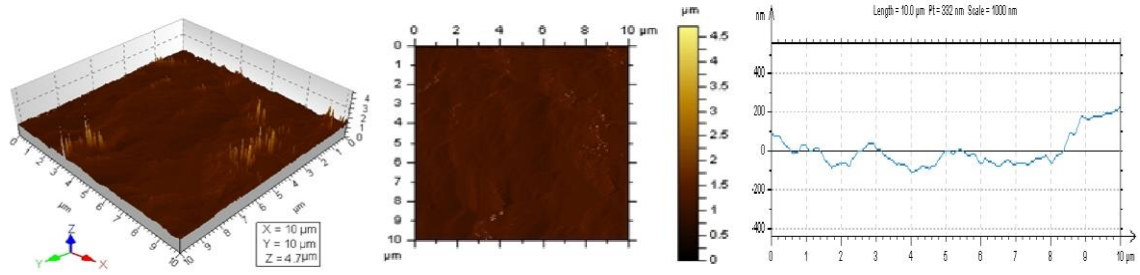

)Velocity: 10 m/s, angle: 60°, distance: 45 mm, erodent discharge: 1500 g/min(Substrate)

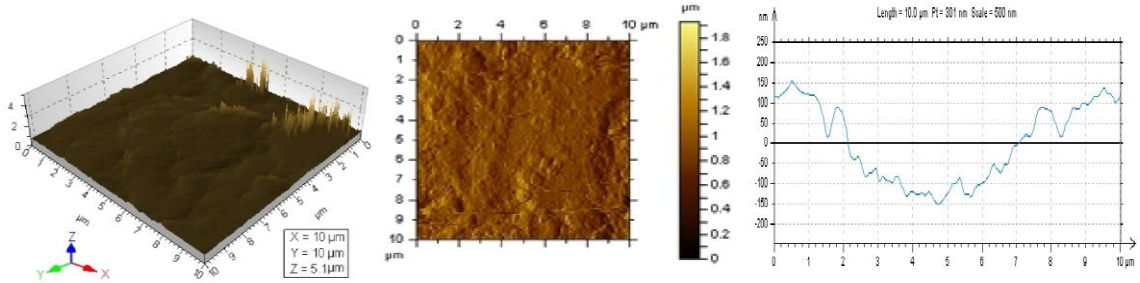

(b) Velocity: 50 m/s, angle: 60°, distance: 45 mm, erodent discharge: 1500 g/min(Coating)

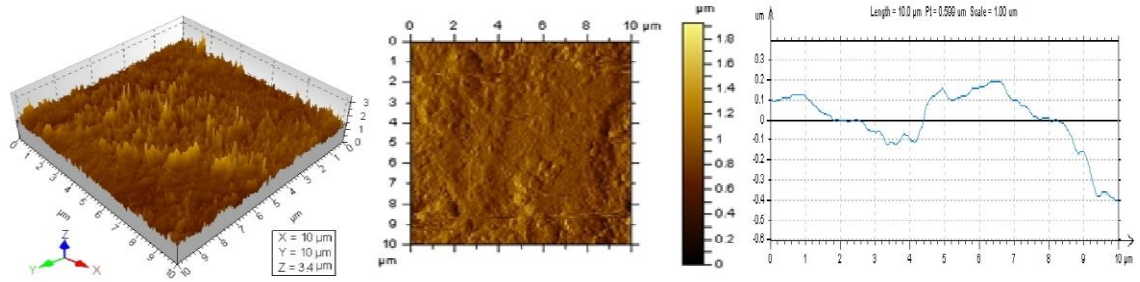

(c)Velocity: 10 m/s, angle: 60°, distance: 45 mm, erodent discharge: 1500 g/min(Substrate)

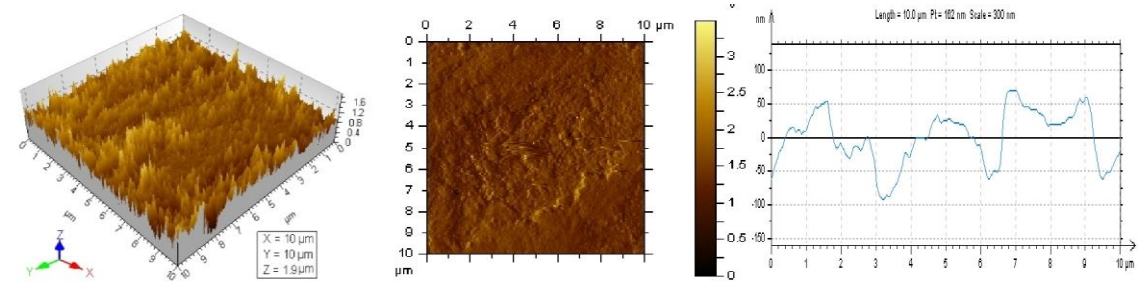

(d) Velocity: 50 m/s, angle: 60°, distance: 45 mm, erodent discharge: 1500 g/min(Coating)

Fig. 10 AFM image of the eroded surface of substrate and coating at low and high water jet velocity conditions

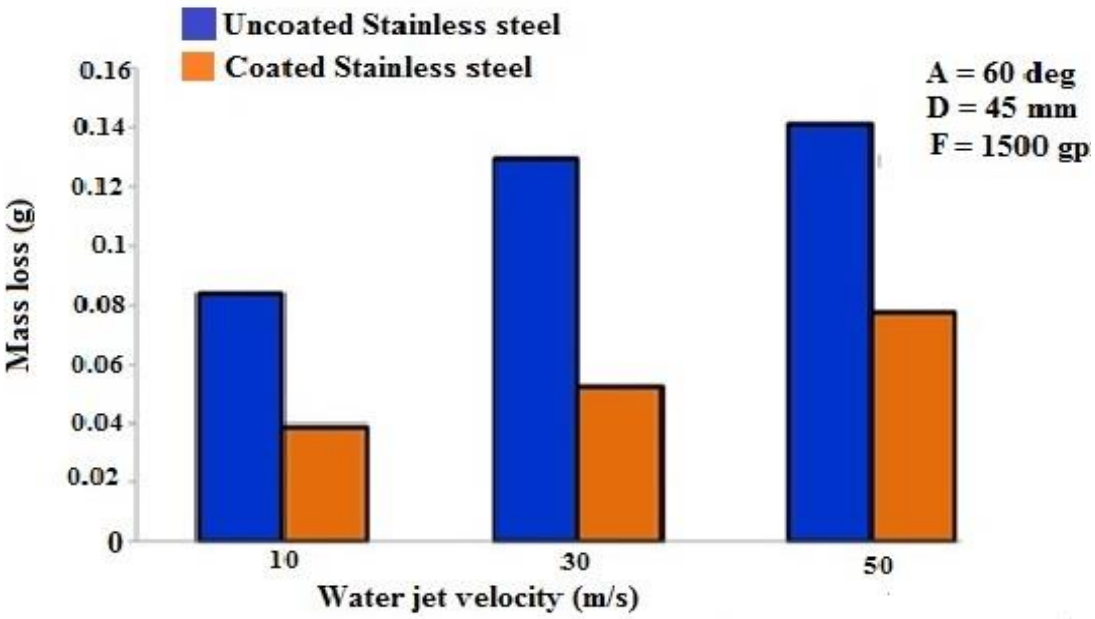

Fig. 11 Effect of water jet velocity on erosion behavior

4.3 Effect of angle of impact of the erosion rate

Under low impact angles, the erodent particle will have the tendency to slide over the surface and as it slides, it will plough the material as observed in Fig.12a. The sequent sliding of the particle will remove the material from the surface; in other words, a certain portion of the volume swept out at low angles of incidence will simply be deformed and displaced in a pouching action. Since the erodent particles are being in contact for long time on the surface during sliding, the wear rate is much high. Because of the different impingement angles of the sand particles, the eroded scars have different lengths and shapes. However, small rubbing action was observed in coated surface at low impingement angles that removes small volume of material as shown in Fig.12b. The micro cutting and wedges seen in SEM images (Fig.12c). At moderate angles, ductile metallic material shows such kind of pattern.

It is evident that at shallow impingement angles, erosion damage is dominated by both splat ejection and plastic deformation of the lamellae. Further, in the plastically deformed areas, grooves or plough marks are often observed. The plastic grooves, in many instances, are similar to scratches produced on coated surfaces by a sharp and hard indenter and they tend to lie along the particle-colliding direction. In the case of shallow angle eroded surfaces. Fig.12d exhibits the dominant material removal mechanisms such as splat ejection, which is caused-by grain lamellar micro-cracking and plastic deformation followed by smearing of the deformed material. The mechanism by which material is removed from a surface upon erosion attack can be either ductile or brittle. In general, the ductile process (stainless steel) is typified by maximum wastage at low impact angles. Most of metallic materials will erode by this mechanism [24].

Metals impacted at higher angles experiences drilling like cutting actions. Hence, Jet hits the target surface with particles makes small lips and plates in eroded uncoated stainless steel as shown in

Fig.12e. On the other hand for the brittle (Cr_3C_2 - NiCr coated stainless steel) ceramic materials the erosion process is featured with maximum wastage at high impact angles, under which erosion occurs by cracking and chipping of surface material [25].

Coating porosity is often located along the lamella boundaries not only will it influence the strength of the inter-lamella but may also initiate micro-cracking and macro cracking leading to the loss of lamellae and thus coating removal. The erosion involved material removal by breaking of the splat boundaries and their pull out along the grooves from the surface. The eroded surfaces revealed broken lamellae and fragmentation as well as large craters in the eroded zone (Fig.12f).

The material removal of stainless steel tested at a 30◦ impact angle was higher than that tested at a 90° of impact angle. Such erosion behavior is typical of ductile materials. In contrast, all the coating eroded greater a material loss at a steep angle ($\alpha = 90°$) than that at a shallow angle ($\alpha = 30°$). Such behavior is typical of brittle materials.

Figures 13 a-f evident of images taken at the eroded surface at low and higher impingement angles. By comparing Ra value, the results are in good agreement with SEM images. It must be noted that this critical angle is not the impact angle of the impinging particle, but rather the effective angle made by the leading face of the particle with the target surface. Cutting will only occur if the orientation of the particle at impact leads to an effective angle greater than the critical angle for cutting. In the case of ploughing, a wave of deformed material is pushed ahead of the sliding particle.

Figures 13 (a-f) shows the surface profilometry suggests that the coating initially deforms plastically, but as the erosion continues a point is reached where the presence of the Cr_3 inhibits further plastic flow. Erosion tests of alloys containing second phase chromium carbides, suggested that the inhomogeneous nature of the plastic flow results in very high strain gradients, which lead to void formation near to, and cracking of, the chromium carbides. These processes were attributed to be the cause of material removal when crack growth has reached a critical extent and the coating fails, probably by spalling. Hence, high undulations in coatings is due to spalling of coatings. Plastic permanent deformation in substrate shows lower undulation during the measurement.

Uncoated specimens **Coated specimens**

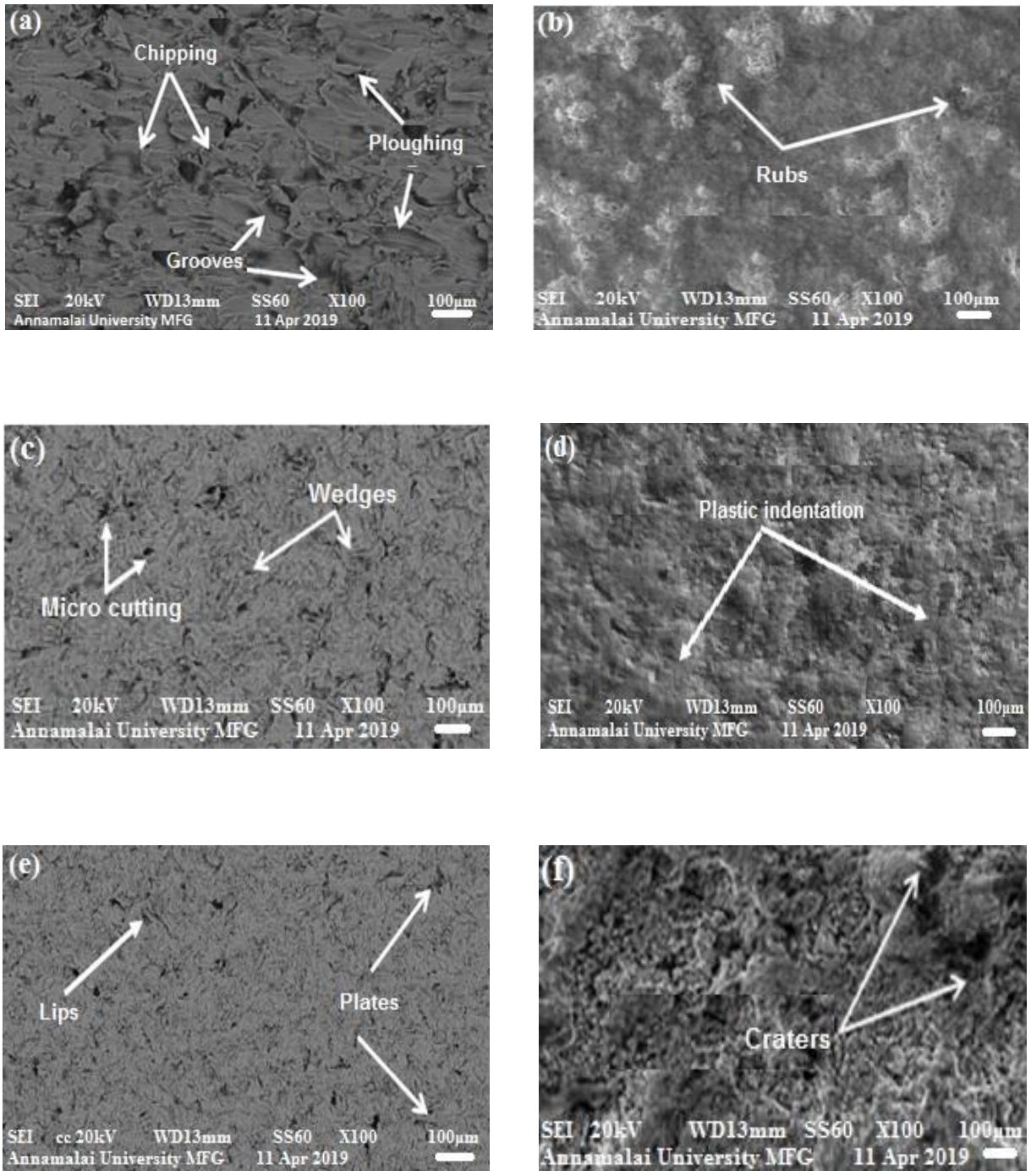

Fig. 12 SEM image of the eroded surface of substrate and coating at various impact angle

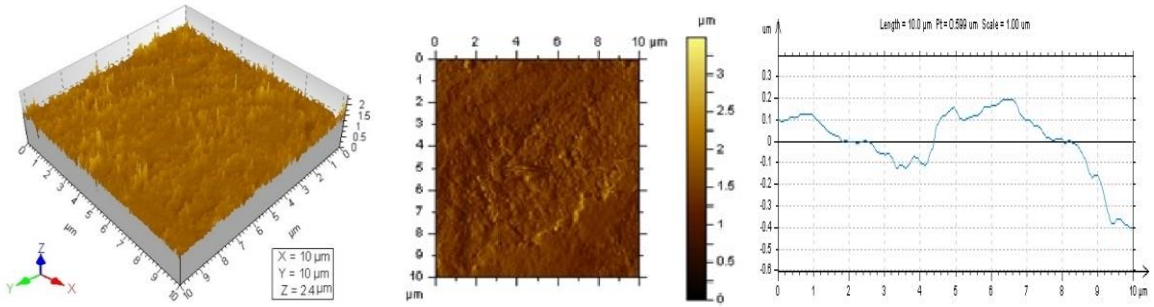

Velocity: 30 m/s, angle: 30°, distance: 45 mm, erodent discharge: 1500 g/min (substrate)

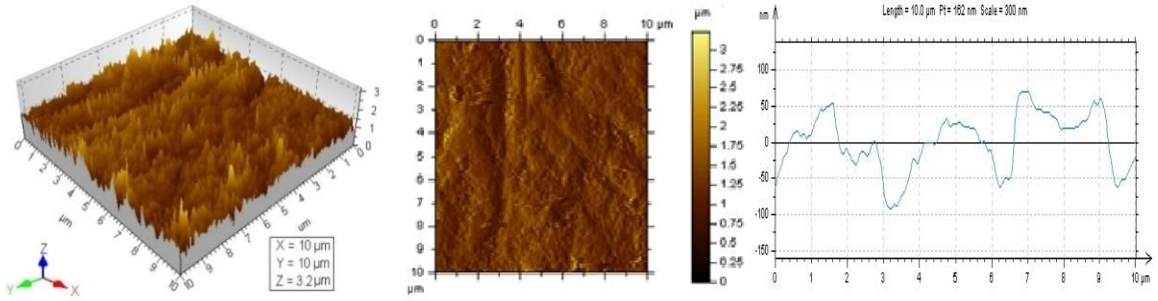

Velocity: 30 m/s, angle: 90°, distance: 45 mm, erodent discharge: 1500 g/min (Coating)

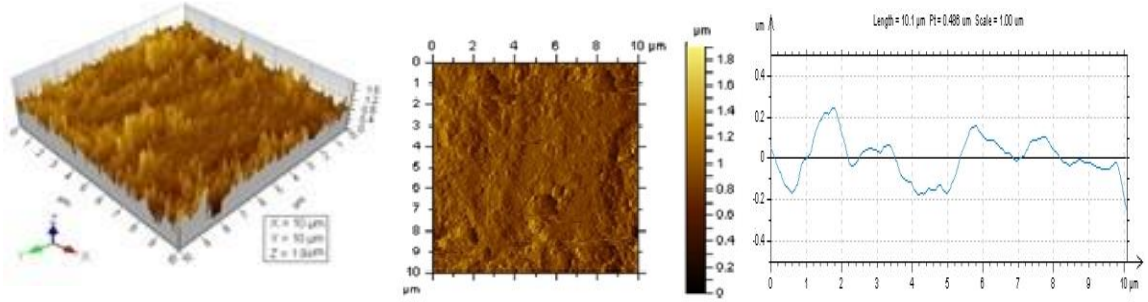

Velocity: 30 m/s, angle: 30°, distance: 45 mm, erodent discharge: 1500 g/min (substrate)

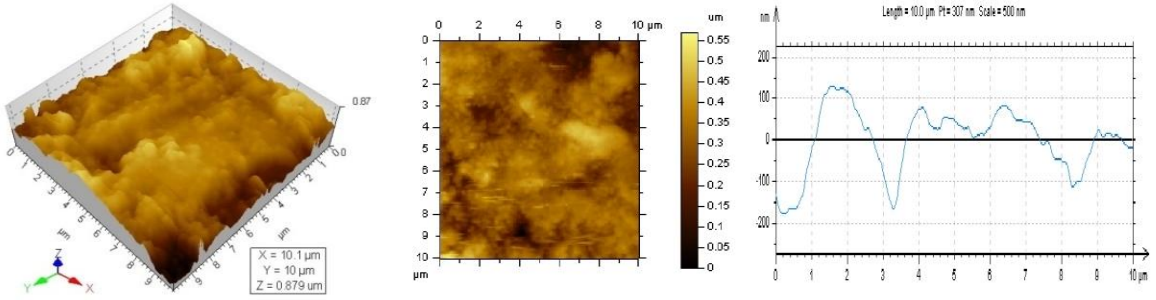

Velocity: 30 m/s, angle: 90°, distance: 45 mm, erodent discharge: 1500 g/min (Coating)

Fig. 13 AFM image of the eroded surface of substrate and coating at low and high impact angle conditions

Figure 14 compares the mass loss occurred on specimens during water jet erosion tests at different impingement angles. It is worth noting that when specimens tested at a 90° angle, despite of higher hardness and more brittle, the coatings had much lower erosion loss compared with stainless steel. This could be attributed for their favourable microstructure with more uniform distribution of

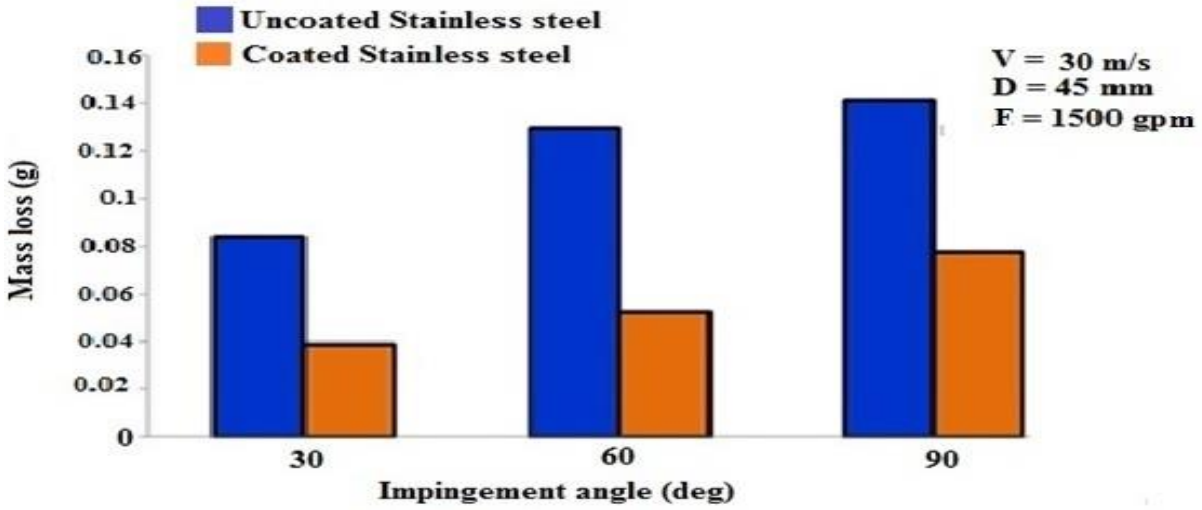

Fig. 14 Effect of water jet impingement angle on erosion behavior

smaller Cr_3C_2 - NiCr particles, lower porosity and oxide content.

4.4 Effect of erodent discharge on erosion rate

The effect of erodent discharge on the erosion scar of the uncoated stainless steel and the coated stainless steel is displayed in Fig. 15.

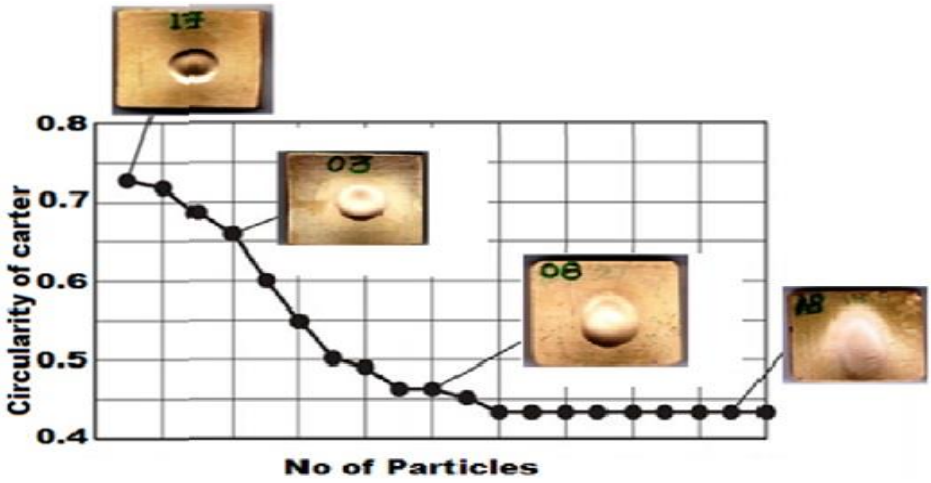

Fig. 15 Effect of erodent discharge on crater formation

Erodent discharge is usually defined as the mass of particles striking the target surface per unit area per unit time. Erosion rates are found to be increasing in a linear manner with increasing erodent discharge and decreases with an increase in the angle of impingement. However, increase in erodent discharge makes an effect on the crater shape and the effect of particles influences on

wear rate. SEM images of eroded specimen shows micro cutting, plouging and plattte-type failures due to the interaction of erodent particles on the target surface as shown in Figure 16.

At low erodent feed rate, the incident energy (impact energy) was higher. When theerodent discharge at impact is reduced, the amount of erosion damage per unit mass of abrasive striking the target increases. When the erodent discharge is low, the mean free path of the water jet erodent particles S is quite long and thus the probability of collision between the rebounding particles and the incident particles is very low. When the particle concentration decreases and the conveying velocity increases there is an increased occurrence of erosion damage. When the erodent discharge value is too high, hydrodynamic particle interactions occur in the nozzle arid becomes more noticeable as the erodent discharge increases further. As the flux increases, the probability of collision between particles increases exponentially and hence the erosion rate would be expected to decrease [26]. This turbulence attenuation increases the water jet spreading rate and causes a faster decay of the jet mean centerline velocity, thereby reducing the erosion rate. From the SEM images, it is observed that the substrate possessed dough marks, Micro cutting and wedge formation as shown in Fig.16 (a, c & e). Cr_3C_2 - NiCr coatings show (Fig. 16 b, d-f) cracking, splat ejections and lamelle spallation. From the water jet erosion test, it is obvious that the erosion rate is low at the highest particle concentrations compared to low flux conditions. This could possibly be explained through a realization that greater numbers of inter-particulate and particle - wall collisions will occur at a higher particle concentration.

AFM images of the eroded specimens are shown in Figs.17 (a-d). At all the erodent discharge levels both substrate and coatings experience material loss. Surface profilometry shows the waviness (R_a) is in higher. Higher R_a level that confirms the material removal from the target surface.

It is thought that the nature of the particle-particle interactions can be divided up into two parts Particle-tube interaction: It is believed that at low fluxes, the interactions that the particles are likely to experience from the time that they are introduced into the water stream are particle-tube interactions which slow the particles down and account for the particle velocity being less than the water jet velocity

Uncoated specimens **Coated specimens**

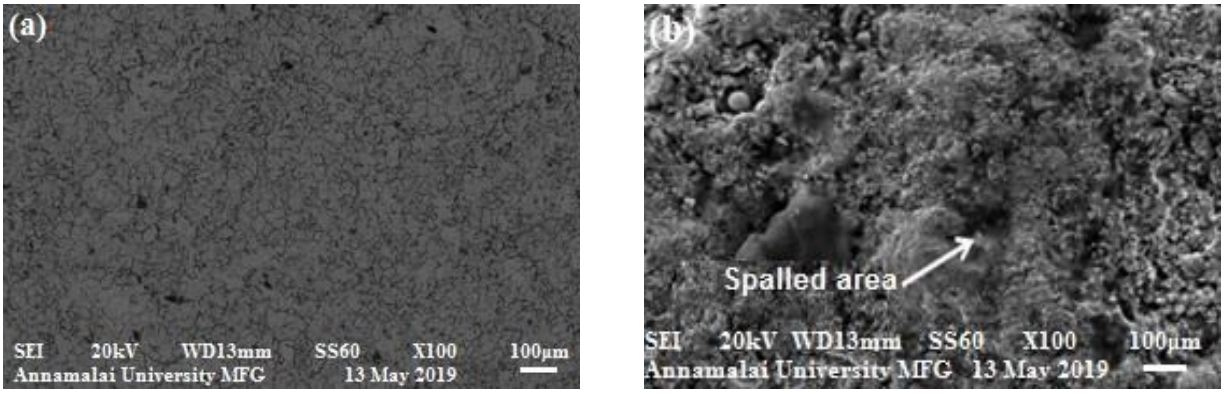

Velocity: 30 m/s angle: 60° deg distance: 45 mm erodent discharge: 500 g/min

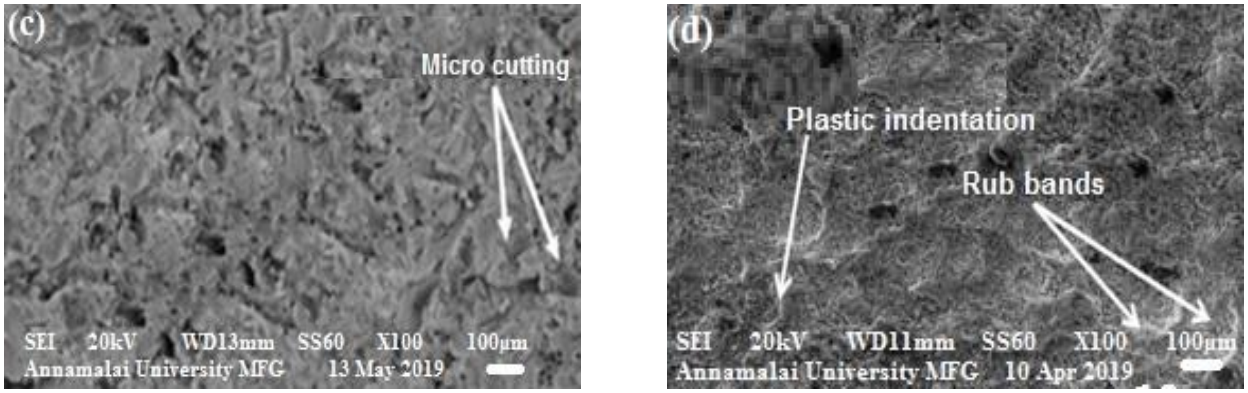

Velocity: 30 m/s angle: 60° deg distance: 45 mm erodent discharge: 1500 g/min

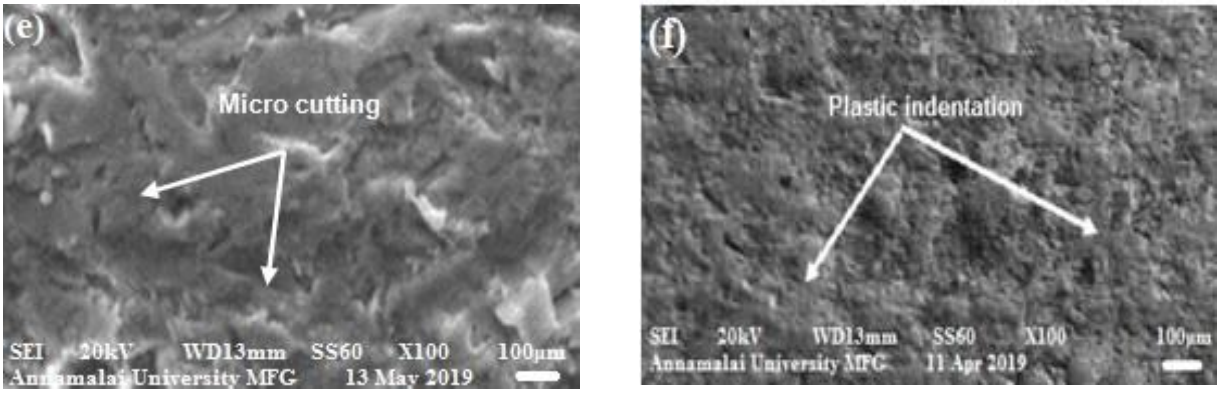

Velocity: 30 m/s angle: 60° deg distance: 45 mm erodent discharge: 2500 g/min
Fig. 16 SEM image of the eroded surfaces of substrate and coating under different erodent discharge

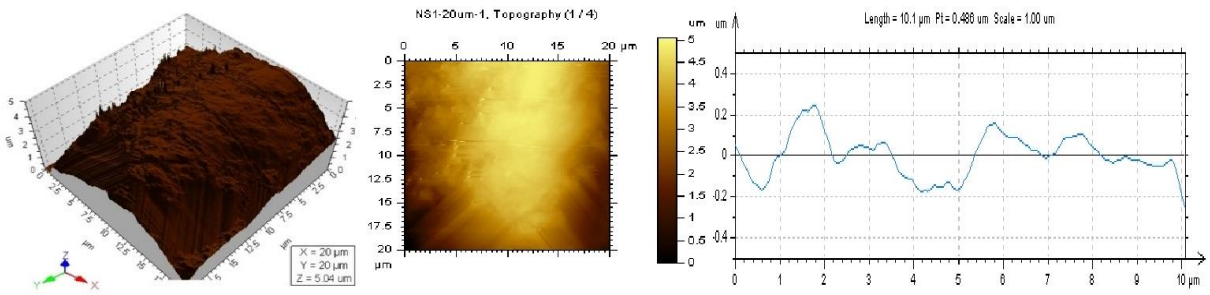

(a) Velocity: 30 m/s angle: 60° distance: 35 mm erodent discharge: 1500 g/min (Substrate)

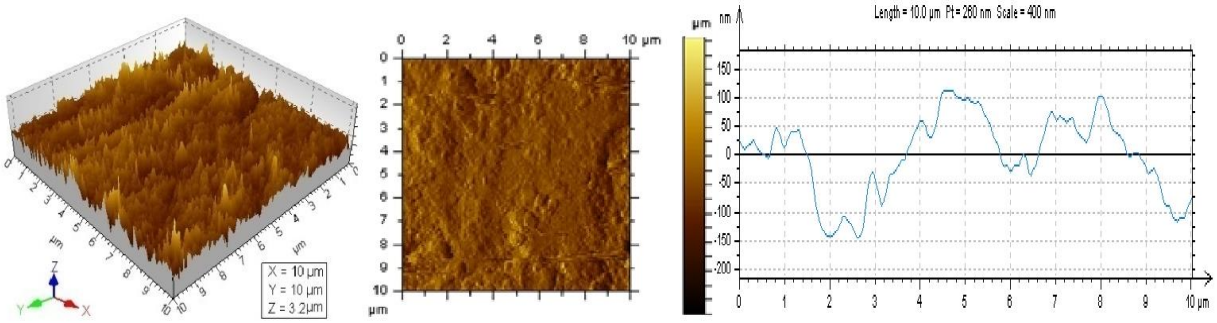

(b) Velocity: 30 m/s angle: 60° distance: 55 mm erodent discharge: 1500 g/min (coatings)

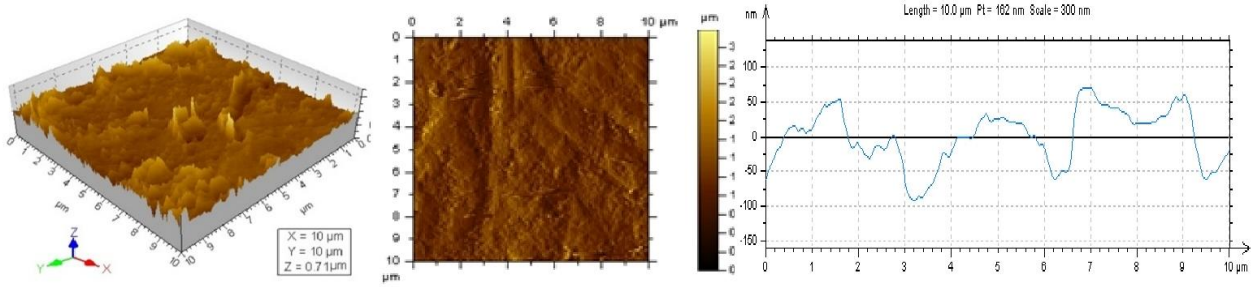

(c) Velocity: 30 m/s angle: 60° distance: 35 mm erodent discharge: 1500 g/min (Substrate)

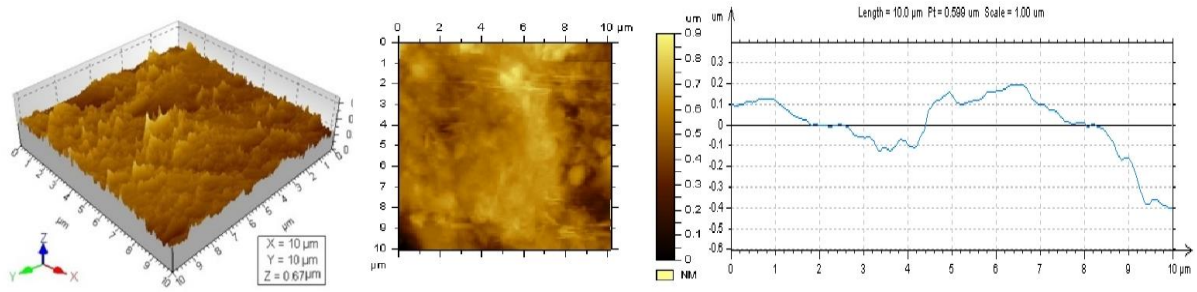

(d) Velocity: 30 m/s angle: 60° distance: 55 mm erodent discharge: 1500 g/min (coatings)

Fig. 17 AFM image of the eroded surface of substrate and coating at low and high erodent discharge

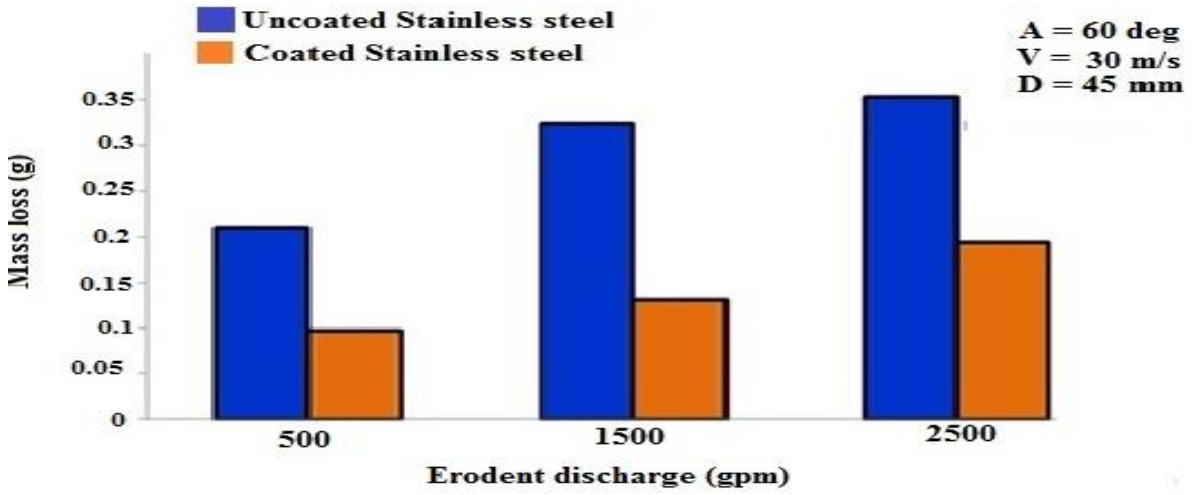

Fig. 18 Effect of erodent discharge on erosion behavior

4.5 Effect of stand-off distance on erosion rate

Stand-off distance is defined as the distance between the face of the nozzle and the sample. Stand-off-distance has been found to have considerable effect on the rate of metal removal. Stand-off distance determines the type of jet impacting on the coating either continues or impact or mixed. Small material removal rates at a low stand-off-distance is due to a reduction in nozzle pressure with decreasing distance, where as a drop in material removal rate at large stand-off-distance is due to a reduction in the jet velocity with increasing distance [27].

When the sample is close to the nozzle, then the erosion pattern can, in the first few seconds of contact, be seen to be like a butterfly in pattern. The central part of the target under the jet is not eroded but there is severe erosion around the edges of the jet diameter, where a grain will see high differential pressures across its width and will be subject to high lateral jet flows. Material removal from the target stainless steel surface through micro cutting and metal cutting features observed on the eroded surfaces as could be inferred from Fig.19 (a-c-d-e).

As the standoff distance increases, the velocity magnitude decreases, Therefore, fine particle are expected to deviate more at shorter standoff distance since the jet radial velocity is higher. At standoff distance of 45 mm is stronger than its influence at standoff distance of 55 mm because more small particles are deviated for the former case. It should be noted that as the standoff distance decreases the static pressure on the substrate increases and, therefore, the percentage of deviated small particles increases. Standoff distance 35 mm, the slope of the curve increases, therefore, erodent of the substrate grows. Micro cutting and metal cutting features observed on the eroded surfaces. Atomic force microscope images taken at the eroded surface are shown in Figs.20a-d.

Uncoated specimens **Coated specimens**

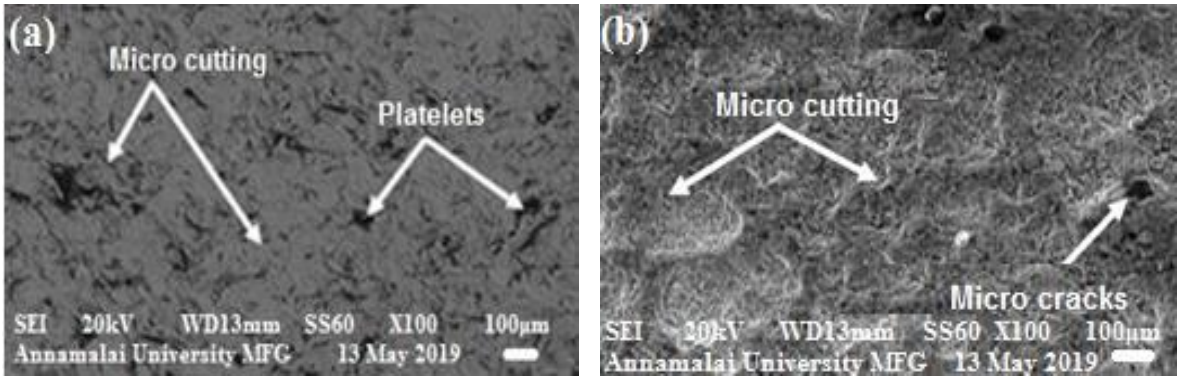

Velocity: 30 m/s, angle: 60°, distance: 35 mm, erodent discharge: 500 g/min

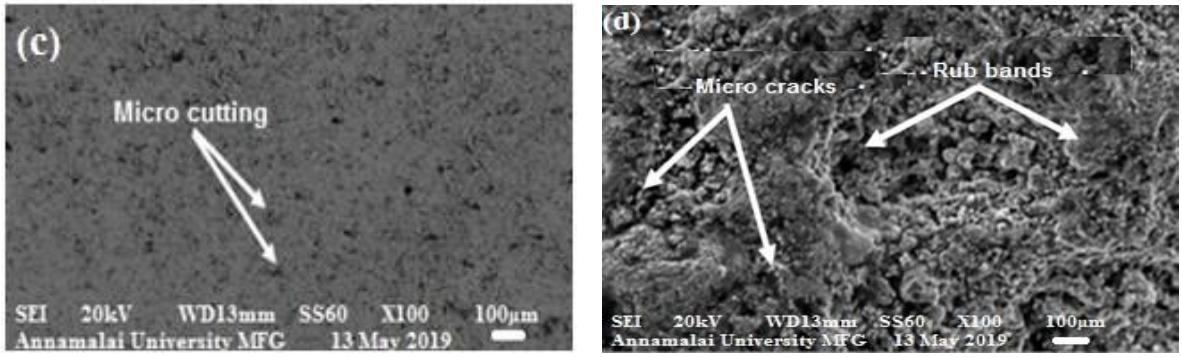

Velocity: 30 m/s, angle: 60°, distance: 45 mm, erodent discharge: 500 g/min

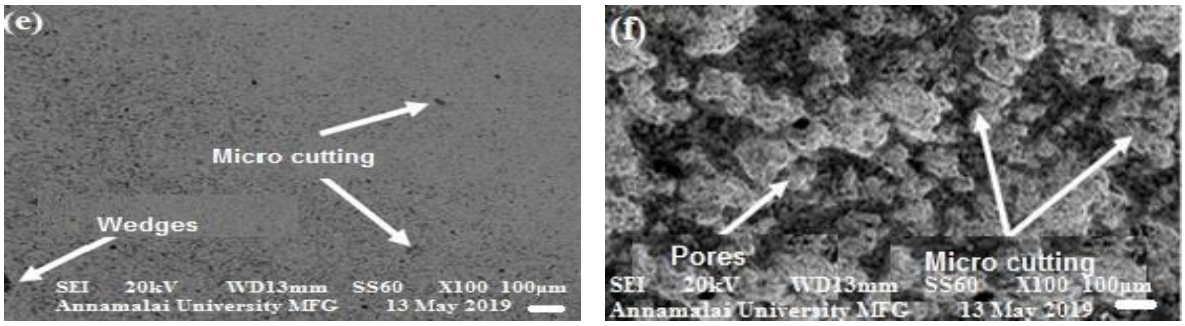

Velocity: 30 m/s, angle: 60°, distance: 55 mm, erodent discharge: 500 g/min

Fig. 19 SEM image of the eroded surfaces of substrate and coating under different stand-off distance

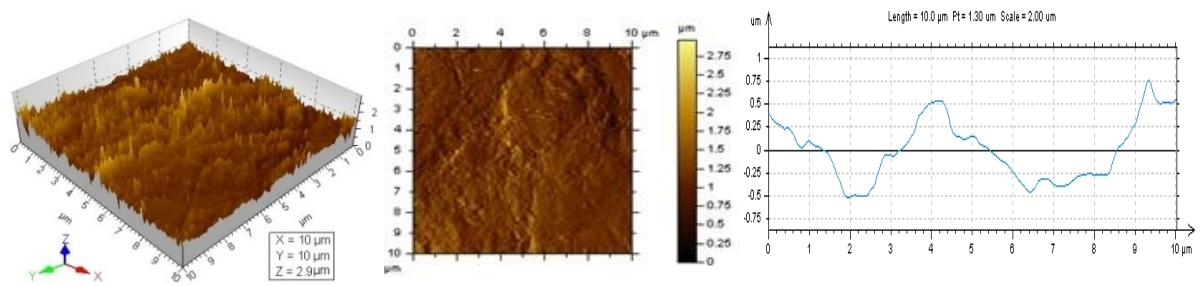

Velocity: 30 m/s, angle: 60°, distance: 45 mm, erodent discharge: 500 g/min (Substrate)

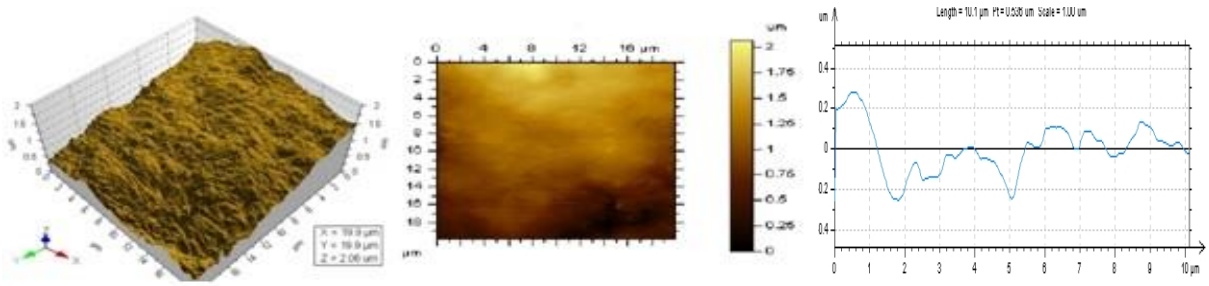

(b) Velocity: 30 m/s, angle: 60°, distance : 45 mm, erodent discharge: 2500 g/min (Coatings)

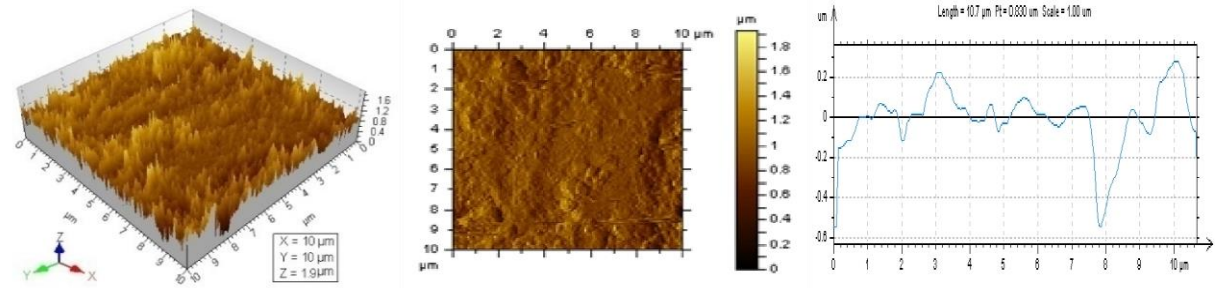

(c) Velocity: 30 m/s, angle: 60°, distance: 45 mm, erodent discharge: 500 g/min (Substrate)

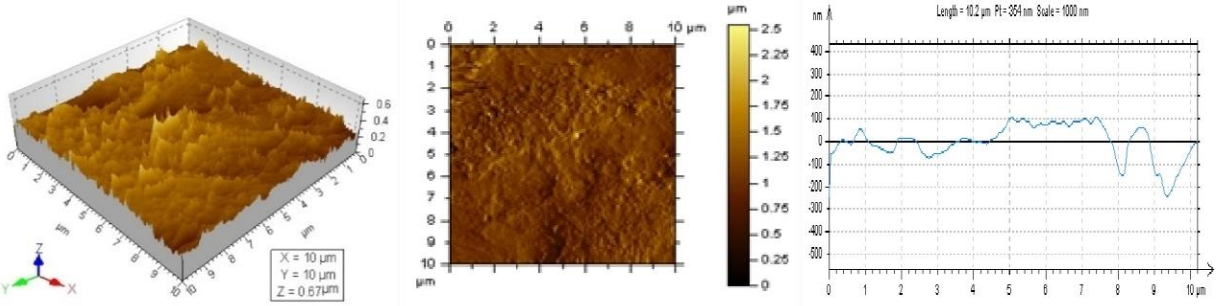

(d) Velocity: 30 m/s, angle: 60°, distance: 45 mm, erodentdischarge: 2500 g/min (Coatings)

Fig. 20 AFM image of the eroded surface of substrate and coating at low and high stand-off distance

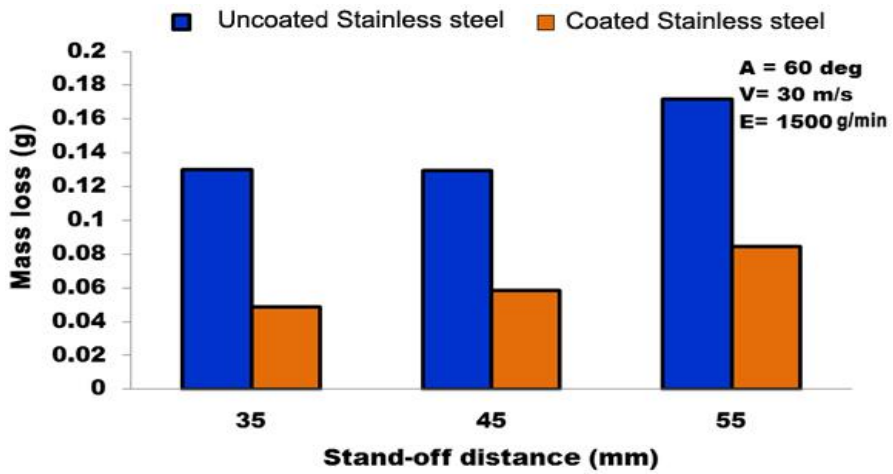

Fig. 21 Effect of stand-off distance on erosion behavior

5.0 CFD Modeling, Analysis and Validation

An attempt has been made to develop the CFD model for water jet erosion test setup, nozzle geometry and fluid domain to predict the erosion rate and to compare the experimental results. The simulations are considered in this work requires complex geometry, lot of memory and time to perform. To avoid complexity, different mesh and setup have been adopted to get the possible results. To perform the simulations, initially 2D nozzle geometry was modeled and revolved in to 3D geometry using Design modeler available in the ANSYS FLUENT software. ANSA meshing is considered as good tool for meshing and used to discrete the nozzle portion and stainless steel samples. The schematic diagram of nozzle, fluid jet direction and nozzle geometry are illustrated in Fig.22. Meshed models of nozzle and specimens are shown in Fig.23 and 24.

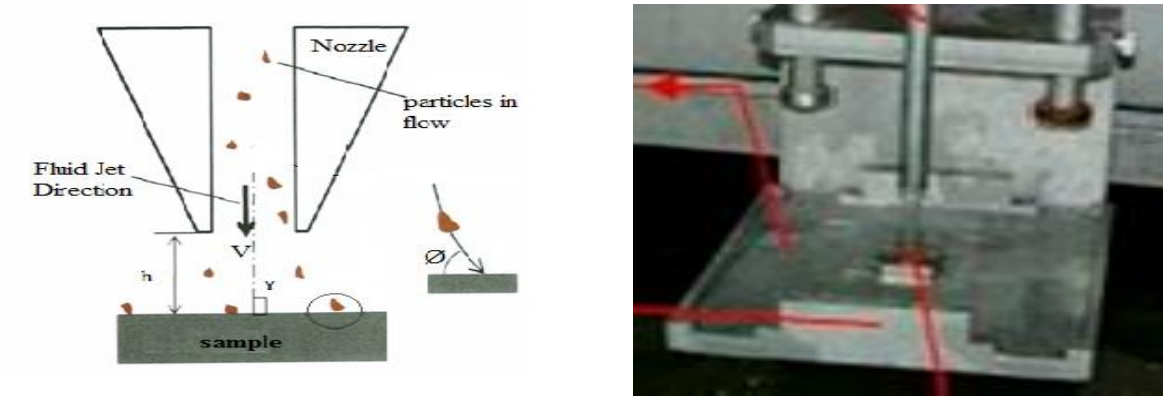

Fig. 22 Schematic diagram of nozzle and experimental setup

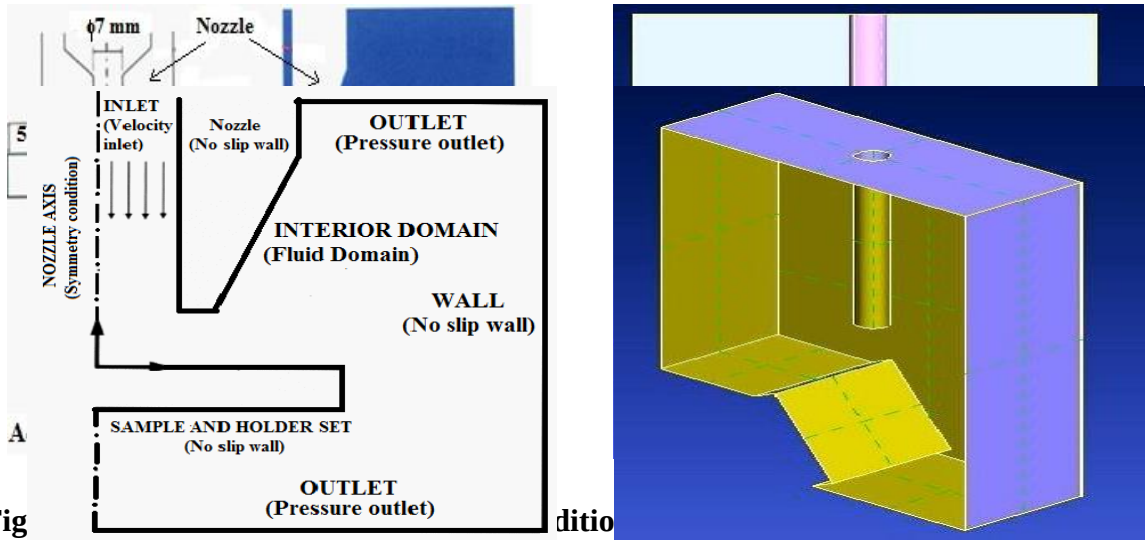

Fig. 24 Developed model after assuming boundary conditions

Table 5 represents the fluid parameters assumed for erosion model available in the DNV module in ANSYS Fluent. After assuming the relevant data first, fluid simulation was performed without activating the DPM. Once fluid simulation is performed in good level and fluid coming nearer to the outlet of the nozzle, the DPM model is activated and particles are released from the inlet, without resolving the fluid. After resolving the fluid, the injected particle were tracked by particle tracking mode to determine the erosion rate at impact on the specimens by software and numerical results were corrected using the following equation,

$$ER_{Impact}\,\frac{\mu m}{Kg} = \frac{(\text{DPM}-\text{Erosion rate})\text{ x }10^{6}}{(84000\text{ x }0.000164)} \quad \ldots\ldots\ldots\ldots\ldots\ldots\ldots\ldots\ldots\ldots(4)$$

Where

Density of stainless steel - 84000 kg/m^3

Mass flow rate of particle - 0.000164 kg/s

Table 6 shows the particle tracking data. To increase the accuracy of the predicted results, Eulerian model with DDPM setup was incorporated to simulate the abrasive wear environment. A thin dense slurry flow with a particle concentration of 400 g/min was assumed for gravitational effects. Accuracy of the available results can be improved by adopting sweep method in the CFD model to increase the no. of elements and nodes and suitably represented in Table 7.

Table 5 Fluid Parameters

Fluid	Water
Thermal	None
Turbulence model	k-ω SST
Wall functions	Automatic
Inlet velocity	5 [m/s]
Fluid density	1000 [kg/m^3]
Outlet relative pressure	0
Wall Boundary	No slip, smooth walls

Table 6 Parameter for particle tracking

Particle diameter	0.25 mm
Particle density	2600 [kg/m^3]
Sand particle definition	Medium Coarse
Particle coupling	One-way
Mass flow	0.000164 [kg/s]
Erosion Model	Det Norske Veritas (DNV)
Diameter function,	K 2e-09
Velocity exponent function, n	2.6
Normal reflection coefficient	0.8
Tangent reflection coefficient	1
Drag law	Morsi and Alexander
Virtual mass force	None
Particle collision	None
Pressure gradient force	Yes
Particle breakup	No
Scale flow rate by face area	Yes

Table 7 Meshing information

Number of elements	1005750
Number of nodes	1036453
Element size [mm]	5
First layer thickness [mm]	0.1
Aspect ratio	13.57
y+	8.7065

Figure 25 shows the meshed model indicates water jet and sample considered for simulation. After assuming coupled multiphase fluid flow simulation and suitable boundary conditions at inlet and exit of the nozzle, the model was simulated by considering continuous fluid flow at inlet and discrete flow at outlet. Table 8 lists the properties for multiphase coupled model. Predicting erosion rate accuracy further improved by introducing ANSYS abrasive model in the existing model that defines solid wall shear stress. Ansys abrasive wear model parameters are listed in the Table 9. Abrasive erosion rate predicted from the model can be corrected by using the given formula,

$$ER_{Abrasive}\ \frac{\mu m}{Kg} = \frac{\tau_{ws.}(\text{DPM}-\text{Erosion rate})\ \text{x}\ [\frac{\alpha_3}{\alpha sp}]\ \text{x}\ 10^6}{(7800\frac{Kg}{m^3}\ \text{x}\ m_{particles})} \quad \text{.....(5)}$$

Where
τ_{ws} is the particle wall shear stress,

(DPM erosion rate) is the KVn values from the definition,

α_3 is the particle volume fraction and

αsp is the packing volume fraction.

$m_{particle}$ is the mass flow rate of particles for a given case and 7800 is the density of stainless steel.
Post processing done by turning on DDPM Eulerian parameter. Calculations pertaining to the erosion rate consists,

$$ER_{Total}\frac{\mu m}{Kg} = ER_{Impact} + ER_{Abrasive} \quad \text{.....(6)}$$

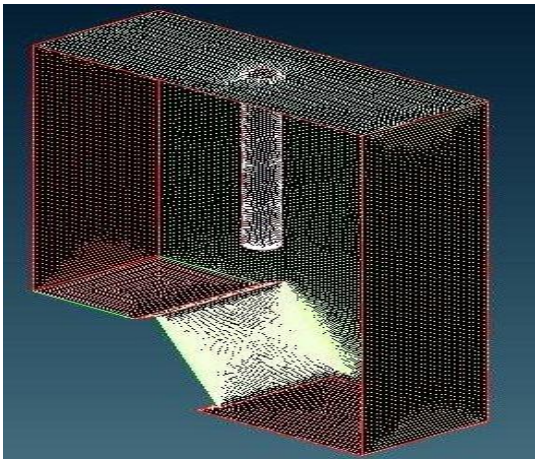

Fig. 25 Meshed model indicates water jet and sample

5.1 Results and Discussion

Figure 26 shows the velocity contour of the simulated water jet impacting over the target kept at different impingement angle to provide the real experimental conditions. From the figure it is inferred that the velocity is increases significantly by passing through the contracted tube and impacting over the target surface at a velocity closer to 100 m/s. The red arrow indicates that the jet is reversed after the impact at 45° angle made with the specimens. For this simulation, the y+ values are sufficiently low, and less than 5. This means that the low turbulence in the fluid flow closer to the wall. Figure 27 shows the y+ values of the simulation and suggests that the transition of jet from the pipe to the exposed area, and expected to have high velocity at the time of impact. After solving the flow field, the particles are released at the inlet. The velocity profile affects

particles trajectories along the domain. The maximum erosion rate is located centre position of the sample at the downstream of the outlet-pipe, and most of the erosion occurs around this region. Erosion is not visible in Figure 28 at 45° wall opposite to the contraction. From the theoretical point of view, specimens exposed to jet could experiences minimum erosion. Hence, the erosion rate is lower at this point. By setting the contour range to a lower level, it is possible to see that erosion also will occur in the 45° contraction. Simulations were carried out at various angles, results show that the maximum erosion occurs at an impingement angle between 60°-90°.

Results obtained from the DNV erosion model, fluid and model domain considers Eulerian model with DDPM to take an account of gravity force affecting the high concentrated particle flow, particles that are sliding and jumping along the pipe wall. Figure 28 show the particles distribution along the pipe is smooth and reaching the target very close to the bottom wall due to the gravitational forces in the –Y direction and hitting the target surface as expected. The slurry flow in this study is settling, heterogeneous slurry flow. The momentum transfer between the particles, fluid and the walls behaves as described. A Lagrangian DPM simulation was performed on the straight pipe with high particle concentration. Results show that the pipe-walls are not exposed to erosion, which is expected from the impact based method.

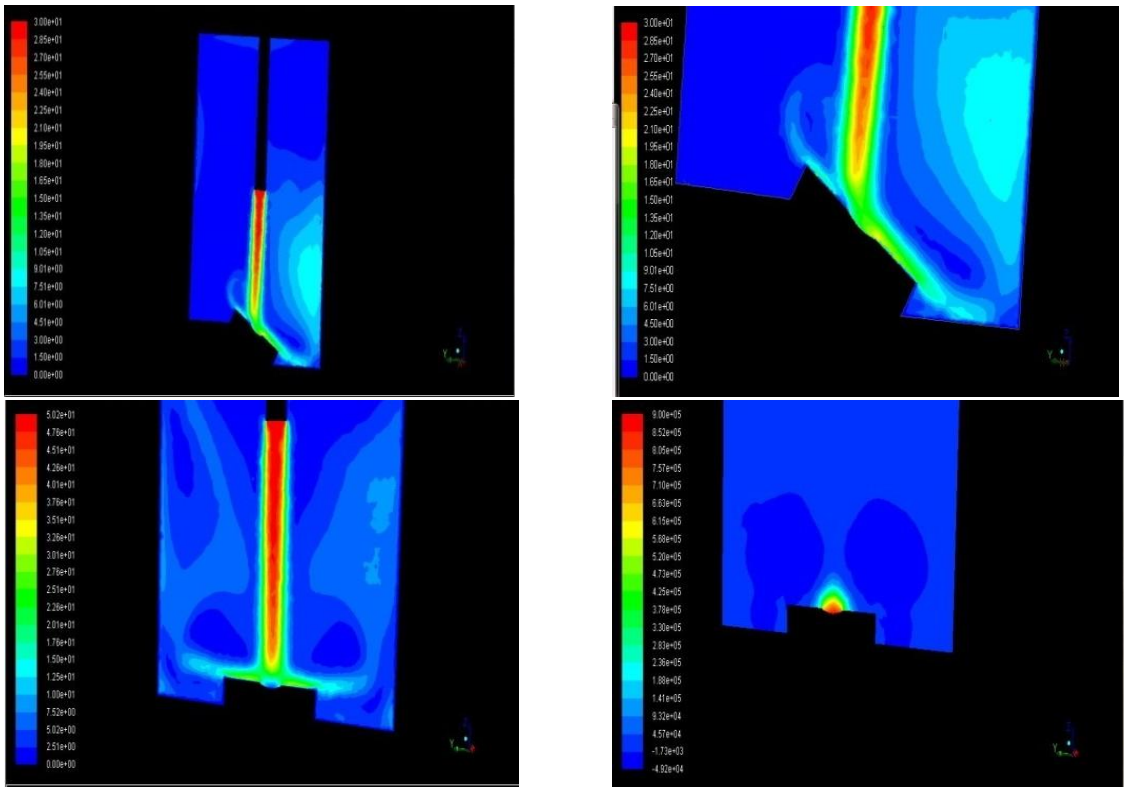

Fig. 26 2D velocity contour for different impingement angle of specimen

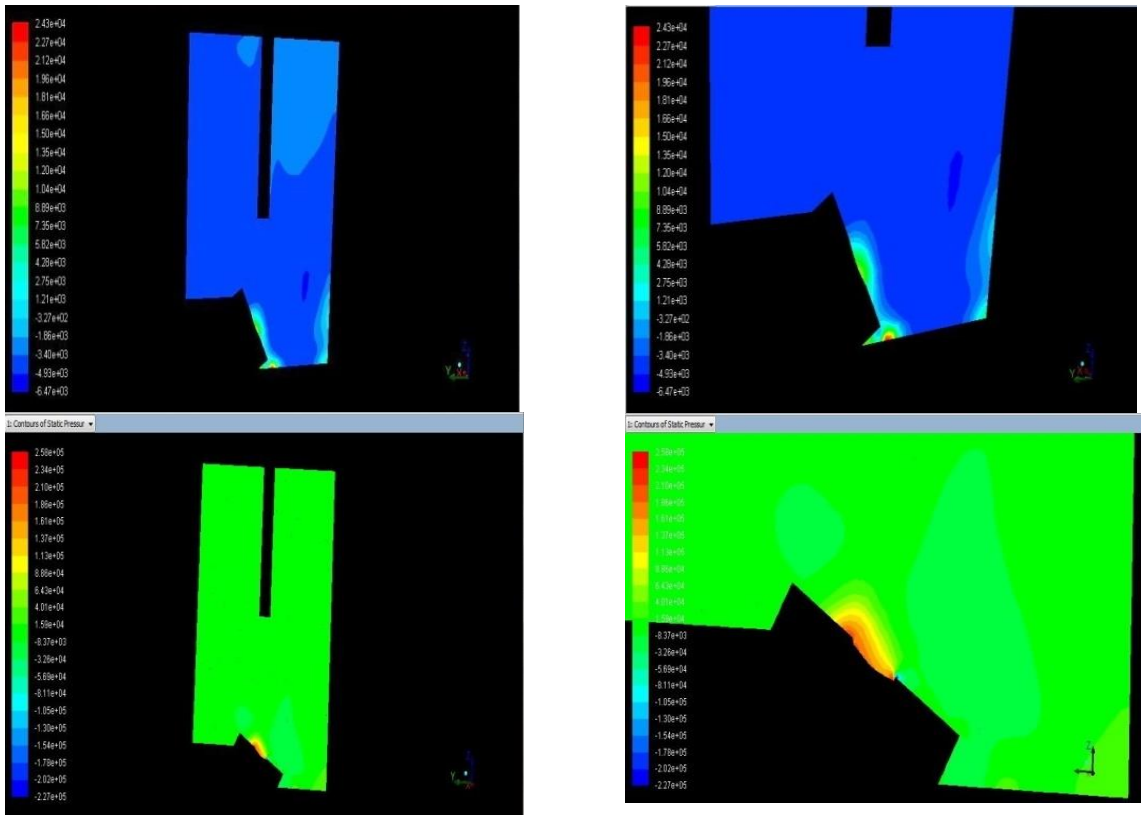

Fig. 27, 2D contour plots show the pressure and velocity

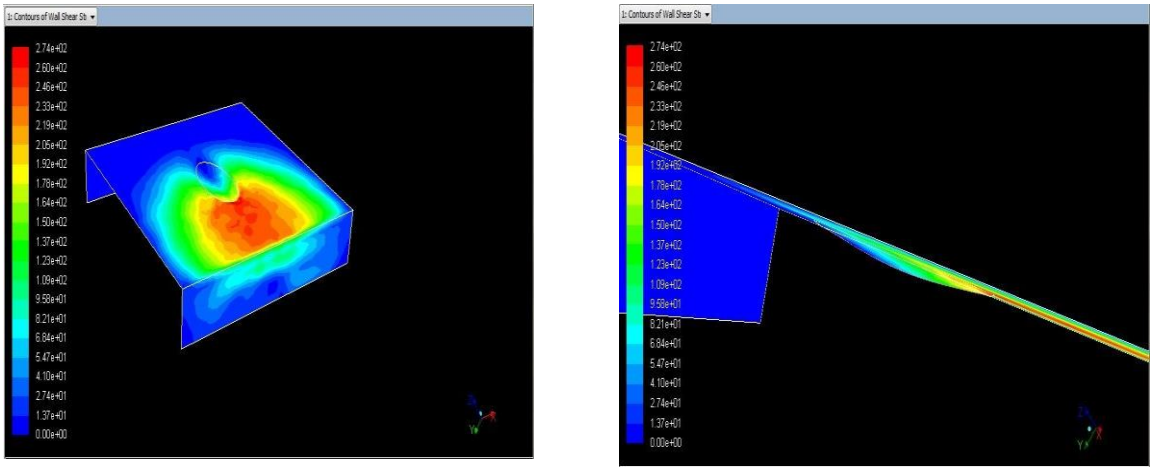

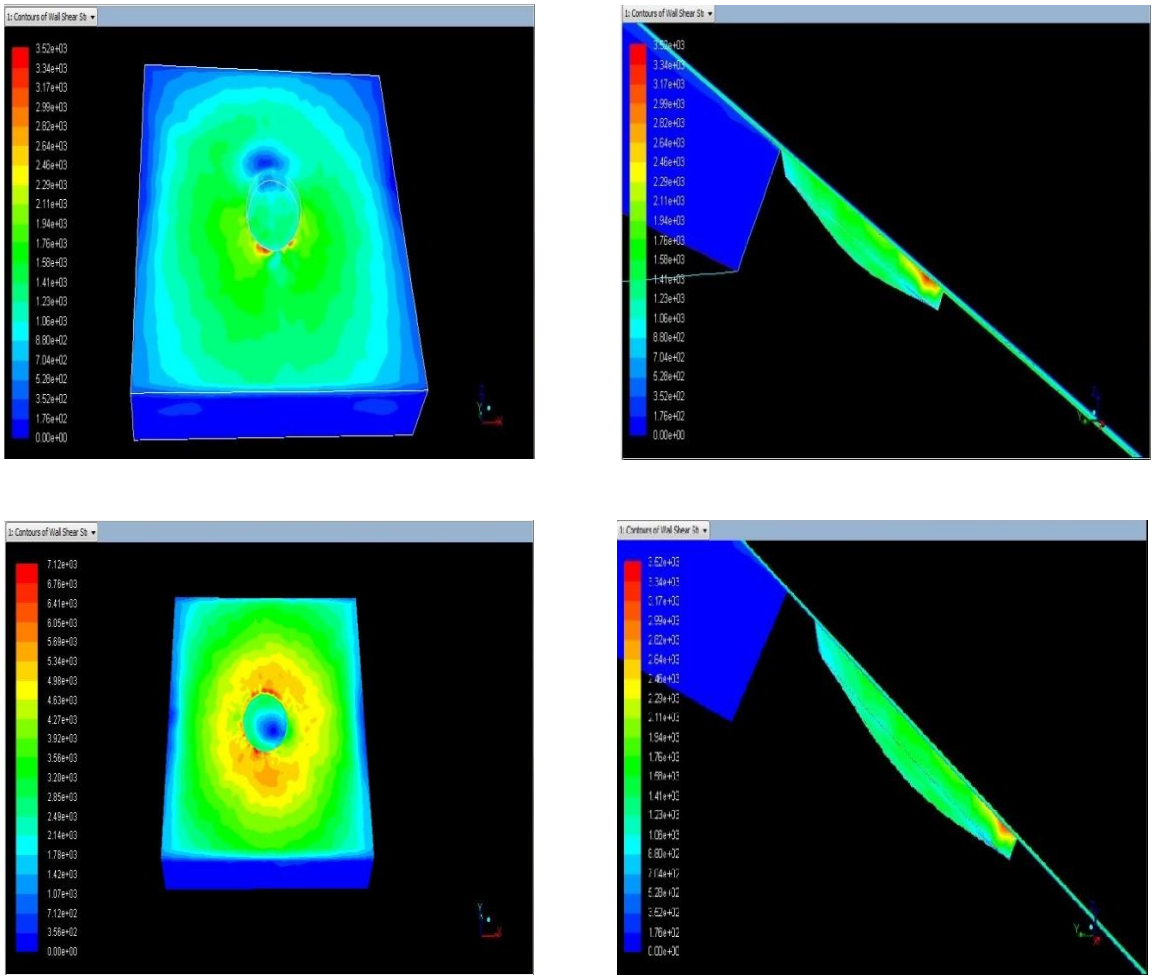

Fig. 28 Contour of the eroded specimen shows maximum erosion

This is a simple geometry where the fluid do not change direction, and therefore the particles will not impact the walls and the model will not capturing the erosion. When particle loading increases, the maximum erosion rate occurs nearer to the contraction because of more particles are present. Since the particle-particle interaction becomes more dominant when the articles are pushed through the contraction and the loading is higher, and there is less space through it. As seen from the graph, 20 vol% and 28 vol% of particles loading condition, the erosion rate is minimized. This is due to the settling of particles at the bottom of sample and particles sliding along the wall. This shows that the higher concentration of particles, the more dominant in the abrasive wear results. Erosion rate is also depending on the particle wall shear stress, particle wall when the shear stress increases erosion rate is also increases. These results show that careful consideration requires when modelling the geometry and assuming the relevant property, otherwise erosion due to particle impact on the target surface becomes less dominant [29-32].

6.0 Conclusions

In this work, Cr_3C_2 - NiCr coatings were developed on stainless steel substrate using high-velocity oxy fuel spray (HVOF) technique. From the experimental results and examination of the microstructures of the coated steel samples before and after erosion, the following conclusions are made:

I. Empirical relationship was established to predict the erosion rate of HVOF sprayed Cr_3C_2-NiCr coatings on stainless steel, incorporating angle of impingement, water jet velocity, standoff distance and erodent discharge. The developed relationship can be effectively used to predict the erosion rate of Cr_3C_2-NiCr coatings on stainless steel at 95% confidence level.

II. Of the four process variables considered, angle of impingement dominates the water jet Erosion rate and followed by water jet velocity, standoff distance and erodent discharge respectively.

III. Ductile stainless steel experiences higher material loss at low impact angle and brittle ceramic based Cr_3C_2 - NiCr coatings eroded at higher angles. Around 40 % improved water jet erosion resistance was observed in stainless steel due to the introduction of HVOF sprayed Cr_3C_2 - NiCr coating in to the stainless steel.

IV. Finite element models were developed to predict the water jet erosion rate without conducting the experiments. From the initial investigation, it is observed that the CFD model is capable to understand the wear behavior of materials under slurry jet impact. Further, these models require suitable approximations to predict the erosion rate numerically.

Acknowledgements

The corresponding author wishes to express his sincere thanks to the Annamalai University for extending facilities to characterize the coatings. The authors also acknowledge the technical support provided by Dr.S.Sree sabari, Post Doctoral Scholar, University of Coimbra, Portugal and Dr.R.Paventhan, Professor, Er.Perumal Manimekalai College of Engineering, Hosur, Tamilnadu.

REFERENCES

1. *S. Hong, Y. Wu, W. Gao, J. Zhang, Y. Zheng, Y. Zheng. Slurry erosion-corrosion resistance and microbial corrosion electrochemical characteristics of HVOF sprayed WC- 10Co- 4Cr coating for offshore hydraulic machinery. Int J Refract Met H., Vol. 74, pp. 7-13, (2018).*

2. *Yuan JH, Ma CW, Yang SL, Yu ZH, Li H. Improving the wear resistance of HVOF sprayed WC-Co coatings by adding submicron-sized WC particles at the splats' interfaces. Surf Coating Technol., Vol. 285, pp.17–23, (2015).*

3. *Goyal DK, Singh H, Kumar H, and Sahni V. Slurry erosive wear evaluation of HVOF spray Cr_2O_3 coating on some turbine steels, J. Therm. Spray Technol., Vol. 21, pp. 838- 851, (2012).*

4. *Hong S, Wu YP, Zheng YG, Wang B. Effect of spray parameters on the corrosion behavior of HVOF sprayed WC-Co-Cr coatings. J Mater Eng Perform., Vol. 23, pp.1434–9, (2014).*

5. *T. Peat, A. Galloway, A. Toumpis, D. Harvey, and W.H. Yang, Performance Evaluation of HVOF Deposited Cermet Coatings Under Dry and Slurry Erosion, Surf. Coat. Technol., Vol. 300, pp. 118-127,(2016).*

6. *S. Hong, Y. Wu, Y. Zheng, B. Wang, W. Gao, J. Lin. Microstructure and electrochemical properties of nanostructured WC-10Co-4Cr coating prepared by HVOF spraying. Surface and Coatings Technology, Vol. 235, pp. 582-588, (2013).*

7. *Sahraoui T, Guessasma S, Jeridane MA. HVOF sprayed WC–Co coatings: microstructure, mechanical properties and friction moment prediction. Mater Des., Vol. 31, pp. 1431–7, (2009).*

8. *K. Murugan, A. Ragupathy, V. Balasubramanian, K. Sridhar. Optimizing HVOF spray process parameters to attain minimum porosity and maximum hardness in WC-10Co-4Cr coatings. Surface and Coatings Technology, Vol. 247, pp. 90-102, (2014).*

9. *Peat T, Galloway AM, Toumpis AI, Harvey D. Evaluation of the synergistic erosion-corrosion behaviour of HVOF thermal spray coatings. Surf Coating Technol.,Vol.299, pp. 37–48, (2016).*

10. *S.B. Mishra, K. Chandra, and S. Prakash, Erosion-Corrosion Performance of NiCrAlY Coating Produced by Plasma Spray Process in a Coal-Fired Thermal Power Plant, Surf. Coat. Technol., Vol. 216, pp. 23-34, (2013).*

11. *C.T. Kwok, F.T. Cheng, and H.C. Man, Synergistic Effect of Cavitation Erosion and Corrosion of Various Engineering Alloys in 3.5% NaCl Solution, Mater. Sci. Eng., Vol. 290(1), pp. 145-154,(2000).*

12. *IL. Baez, CAP. Salas, JM. Saldaña, LGT. Martinez. Effects of the Modification of Processing Parameters on Mechanical Properties of HVOF Cr_2C_3-25NiCr Coating. Journal of Thermal Spray Technology, Vol. 24, pp. 938-946, (2015).*

13. *S. Hong, Y. Wu, Q. Wang, G. Ying, G. Li, W. Gao, B. Wang, and W. Guo, Microstructure and Cavitation–Silt Erosion Behavior of High-Velocity Oxygen–Fuel (HVOF) Sprayed Cr_3C_2-NiCr Coating, Surf. Coat. Technol., Vol. 225, pp. 85-91, (2013).*

14. *G.-C. Ji, C.-J. Li, Y.-Y. Wang and W.-Y. Li, "Microstructural characterization and abrasive wear performance of HVOF sprayed Cr3C2-NiCr Coating," Surf. Coat. Technol., Vol. 200, pp. 6749-6757, (2006).*

15. *ASTM B276-05 Standard test method for apparent porosity in cemented carbides, annual book of ASTM standards, ASTM international-2010.*

16. *Shahi A S and Pandey S. Modeling of the effects of welding conditions on dilution of stainless steel claddings produced by gas metal arc welding procedures. J Mater Process Technol., Vol. 196 (1), pp.339-34, (2008).*

17. *Kumar S, Kumar P and Shan H S. Effect of evaporative pattern casting process parameters on the surface roughness of Al-7% Si alloy castings. J Mater Process Technol., Vol. 182(1), pp. 615-623, (2007).*

18. *D.K. Goyal, H. Singh, and H. Kumar, An Overview of Slurry Erosion Control by the Application of High Velocity Oxy Fuel Sprayed Coatings, J. Eng. Tribol., Vol.225, pp. 1092-1105, (2011).*

19. *L. Thakur and N. Arora, A Study on erosive Wear Behavior of HVOF Sprayed Nanostructured WC-Co-Cr Coatings, J. Mech. Sci. Technol., Vol. 27(5), pp. 1461-1467, (2013).*

20. *A. Kumar, A. Sharma, and S.K. Goel, Erosion Behaviour of WC-10Co-4Cr Coating on 23-8- N Nitronic Steel by HVOF Thermal Spraying, Appl. Surf. Sci., Vol. 370, pp. 418-426, (2016).*

21. *Jianhua zhao, Aibin ma, Xiulin ji , Jinghua jiang and Yayun bao. Slurry erosion behavior of AlxCoCrFeNiTi0.5 high entropy alloy coatings fabricated by laser cladding. Metals. Vol. 8(2), pp. 1-12, (2018).*

22. *K.S. Tan, R.J.K. Wood, and K.R. Stokes, The Slurry Erosion Behaviour of High Velocity Oxy-Fuel (HVOF) Sprayed Aluminium Bronze Coatings, Wear, Vol. 255, pp. 195-205,(2003).*

23. *P. Singh, A. Bansal, and D.K. Goyal, Erosion wear Evaluation of HVOF Sprayed WC-12Co Coating on Some Pipeline Materials Using Taguchi Approach, Kovove Mater., Vol. 57, pp. 113-120, (2019).*

24. *A.K. Jha, R. Batham, M. Ahmed, A.K. Majumder, O.P. Modi, S. Chaturvedi, and A.K.*

Gupta, Effect of Impinging Angle andRotating Speed on Erosion Behavior of Aluminum, Trans. Nonferrous Met. Soc., Vol. 21, pp. 32-38, (2011).

25. *B.S. Mann, High-Energy Particle Impact Wear Resistance of Hard Coatings and Their Application in Hydroturbines, Wear, Vol. 237, pp. 140-146, (2000).*

26. *H.S. Grewal, S. Bhandari, and H. Singh, Parametric study of Slurry-Erosion of Hydroturbine Steels with and Without Detonation Gun Spray Coatings Using Taguchi Technique, Metall.Mater. Trans. A, Vol. 43(9), pp. 3387-3401, (2012).*

27. *S. Kaushal and S. Singh, Slurry Erosion Behavior of Plasma Sprayed Coating on Turbine Steel, Ind. Lubr. Tribol., Vol. 71(1), pp. 1-9, (2019).*

28. *H. Grewal, A. Agrawal, and H. Singh, Slurry Erosion Mechanism of Hydroturbine Steel: Effect of Operating Parameters, Tribol. Lett., Vol. 52(2), pp. 287-303, (2013).*

29. *H. Grewal, A. Agrawal, and H. Singh, Design and Development of High-Velocity Slurry Erosion Test Rig Using CFD, J. Mater.Eng. Perform., Vol. 22(1), pp. 152-16, (2013).*

30. *Li M, and Christofides P D. Computational study of particle in-flight behavior in the HVOF thermal spray process. Chem Eng Sci. Vol. 61(19), pp. 6540-6552, (2006).*

31. *Jae Hyung Kim, Hyung GounJoo, Kang Yong Lee. Simulation of solid particle erosion inWC-Ni coated wall using CFD. J Mater Process Tech. Vol. 224, pp. 240-24, (2015).*

32. *Bernd Schilder, Andre Garling, Fabian Reimer, Matthias Hamann, Rainer Joos, Jens Hüger, Matthias Pöhlmann & Thomas Lampke. CFD enhanced thermal spray process for coating of cylinder bores of car engines. J Therm Spray Technol., Vol. 29, pp. 546–559, (2020).*